

Numerical Study on High Angle-of-Attack Pitching Moment Characteristics of Slender-Bodied Reusable Rocket

Takuya Aogaki¹ and Keiichi Kitamura²
Yokohama National University, Yokohama, Kanagawa, Japan, 240-8501

and

Satoshi Nonaka³
JAXA, Sagami-hara, Kanagawa, Japan, 252-5210

The development of a fully reusable vertical-takeoff-and-vertical-landing (VTVL) rocket is indispensable for reducing space transportation costs. However, there are many technical issues associated with such vehicles, such as the safe execution of a turnover maneuver during return flight. It is known that a relatively desirable pitching moment characteristic for turnover can be accomplished by employing a slender body configuration, but the reason for this is not well understood. In this study, we carried out a delayed detached-eddy simulation (DDES) on the aerodynamic characteristics of such a slender-bodied reusable rocket for angles of attack between 0 and 180 degrees using unstructured compressible computational-fluid-dynamics (CFD). We also conducted inviscid calculations in order to distinguish the pitching moment contribution of the body configuration itself from the effects of viscosity and turbulence. It was found that two types of vortices were formed at 0-90 degrees, and also these vortices affected the pitching moment distribution. We also observed three types of vortices generated at 90-180 degrees. Combined with the results of the inviscid simulation, we concluded that the pitching moment characteristic is greatly impacted by the behaviors of these vortices and bubbles.

Nomenclature

a = speed of sound

¹ Graduate Student, Graduate School of Engineering, 79-5 Tokiwadai, Hodogaya, and Student Member.

² Associate Professor, Graduate School of Engineering, 79-5 Tokiwadai, Hodogaya, and Senior Member.

³ Associate Professor, Institute of Space and Astronautical Science, 3-1-1 Yoshinodai, Chuoku, and Senior Member.

C_m	=	pitching moment coefficient
e_T	=	total energy per unit mass
F_x	=	axial force
F_z	=	normal force
L	=	body length
M	=	Mach number
M_y	=	pitching moment
Pr	=	Prandtl number
p	=	static pressure
q	=	dynamic pressure
Re	=	Reynolds number
S_{base}	=	base (reference) area
$ S $	=	Euclidean norm of the strain-rate tensor
T	=	temperature
U	=	flow velocity
u, v, w	=	velocity components in body-fixed coordinates
x, y, z	=	body-fixed coordinates
δ	=	Kronecker's delta
κ	=	thermal conductivity
μ	=	viscosity
ρ	=	density
τ	=	stress tensor
$ \Omega $	=	Euclidean norm of the vorticity tensor

Subscripts

i	=	value at a cell
t	=	turbulent
∞	=	freestream value

I. Introduction

IN order to realize future space markets such as space elevators and space tourism, we must accomplish many goals, such as reducing the cost and increasing the frequency of space transportations. A fully reusable vertical-takeoff-and-vertical-landing (VTVL) rocket [1] is considered capable of achieving these goals, and a significant amount of research focusing on this rocket has been conducted at the Institute of Space and Astronautical Science/Japan Aerospace Exploration Agency (ISAS/JAXA). So far, many types of reusable rockets have been proposed and studied globally [1-5], and each type has its advantages and disadvantages. However, VTVL type has a significant advantage over other types such as horizontal-takeoff-and-horizontal-landing (HTHL) type, as a VTVL rocket needs neither large wings nor runways, since it is launched by a rocket engine - this enables us to save significant cost.

Two methods for the return flight of such vehicles can be considered; Base-Entry and Nose-Entry, as shown in Fig. 1. It is known from the previous study [6] that Nose-Entry generates a higher lift-to-drag ratio than Base-Entry, allowing for a more slender configuration. On the other hand, Base-Entry requires a low fineness ratio to generate a high lift-to-drag ratio in flight before landing, which consequently increases the drag coefficient during launch. Therefore, Nose-Entry is considered more suitable for a reusable rocket vehicle [6].

In the case of Nose-Entry, a turnover maneuver is executed during the return flight. This maneuver changes the attitude of the vehicle from a nose-first to a base-first orientation using aerodynamic forces acting on the vehicle. This then enables the vehicle to decelerate and achieve a soft landing using its main engine thrust. The pitching moment characteristics of a slender body vehicle during the turnover are shown in Fig.2. The pitching moment is positive for angles of attack (AOAs) between 0 and 90 degrees (designated as “Forward” AOAs hereafter). Therefore, a nose-up moment acts on the vehicle in this region, meaning that the angular velocity of the vehicle is increased. On the other hand, the pitching moment is negative for AOAs between 90 to 180 degrees (“Backward” AOAs). Therefore, a nose-down moment acts on the vehicle in this region, meaning that the angular velocity of the vehicle is decreased. If the area under the nose-up moment curve (Area1 in Fig. 2) and that of the nose-down moment curve (Area2 in Fig. 2) are nearly equal, a stable turnover maneuver can be executed [7]. Thus, it is important to clarify pitching moment characteristics of slender bodies at AOAs between 0 and 180 degrees in order to accomplish a safe and stable turnover.

Many studies investigating aerodynamic characteristics of slender bodies at high angle of attack have been conducted [8-10], but only a limited number of these studies focus on AOAs of more-than-90-degrees or pitching moment characteristics. In Jernell’s experiment [11], aerodynamic characteristics of slender bodies with various cross-

sections and fineness ratios were explored for AOAs between -5 and 185 degrees and at supersonic Mach numbers between 1.50 and 2.86. However, the body configurations and the Mach numbers investigated in the study [11] were completely different from our those investigated in the present study of subsonic flows. Additionally, detailed flowfields were not described in [11]. Jorgensen [12] presented procedures for estimating aerodynamic coefficients of slender bodies for AOAs between 0 and 180 degrees as a function of Mach number, Reynolds number, and angle of attack by Newtonian theory. This process is applicable to our configuration and conditions, but its reliability is questionable, as the Newtonian theory does not account for the viscous and turbulent effects.

Similar studies were also conducted in [7, 13-16]. Nonaka et. al. [7] investigated pitching moment characteristics on many slender body configurations for AOAs between 0 and 180 degrees. They [7] reported that cone-conical frustum configuration reduced the difference between maximum and minimum pitching moment values, in comparison to a cone-cylinder configuration (if such a difference in pitching moment is large, the angular velocity during turnover becomes too high to control). Kuzuu et. al. [13, 14] demonstrated flowfields and aerodynamic characteristics of a cone-conical frustum configuration for AOAs between 0 and 180 degrees numerically. In their studies [13, 14], flow conditions were the similar to those in the present study, but the aftbody configuration is slightly different; in these previous studies the cross-section was always circular along the entire length of the body, whereas in the present study it gradually transitions from circle to curved square. In addition, the number of cells was limited to about 3.2 million (approximately 10 % of the numbers of nodes used in the mesh in the present study), and because of this, the flowfields did not appear to be predicted accurately. Shimojima [15] and Kinami [16] experimentally examined pitching moment characteristics of several cone-frustum configurations (by changing the aftbody configuration from conical frustum used in [7, 13, 14]) and found that the difference of the areas between nose-up moment and nose-down moment was minimized when the aftbody configuration with a square-like cross-section was used, as shown in Fig.3. This result indicates that this configuration is the most suitable as a baseline (without aerodynamic devices) configuration of the reusable rocket vehicle from the standpoint of the above-mentioned desirable pitching moment characteristic for the turnover. However, the relationship between the flowfields and the pitching moment characteristics is not well understood as it is difficult to visualize detailed flowfields in experiments. In this study, we numerically conduct flow computations for AOAs between 0 and 180 degrees around this cone/pyramidal-frustum-like (*slender-bodied*) reusable-rocket-configuration to acquire aerodynamic characteristics, visualize the flow, and relate the pitching moment characteristics to the flowfields. Even though the order of magnitude

of practical Reynolds number of such rockets is considered to be $O(10^7)$ or more, the investigation of aerodynamic characteristics at low Reynolds numbers such as wind-tunnel models is important as a basic research. Thus, in this study, the freestream Reynolds number is set to $Re_\infty = 6 \times 10^5$, which corresponds to the condition of the reference experiments [15, 16]. Although we focus on a specific configuration, aerodynamic findings, such as the effect of angle of attack are applicable to other slender body vehicles.

This paper is organized as follows: Section II will introduce numerical methods and conditions; Section III is dedicated to the computed results and discussions; Finally, in Section IV, the paper will be summarized.

II. Numerical Setup

A. Reusable rocket configuration

Figure 4 shows the body configuration we used in this study. This configuration is composed of nose cone and frustum-like aftbody. The cross-section of the aftbody changes gradually from circle to curved square (with increasing area). We selected this configuration in this study because a suitable pitching moment characteristic for the turnover maneuver can be obtained, as described in [15, 16]. The body length is $L = 307.2$ mm, the base area is $S = 3770.6$ mm², and the fineness ratio ($= L/\sqrt{S}$) is 5.0.

B. Governing equations

The governing equations are the three-dimensional compressible Navier-Stokes (Eq. (1a)) or Euler (Eq. (1b)) equations.

$$\frac{\partial Q}{\partial t} + \frac{\partial F e_k}{\partial x_k} = \frac{1}{Re} \frac{\partial F v_k}{\partial x_k} \quad (1a)$$

$$\frac{\partial Q}{\partial t} + \frac{\partial F e_k}{\partial x_k} = 0 \quad (1b)$$

$$Q = \begin{pmatrix} \rho \\ \rho u_l \\ e_T \end{pmatrix}, F e_k = \begin{pmatrix} \rho u_k \\ \rho u_l u_k + p \delta_{lk} \\ (e_T + p) u_k \end{pmatrix}, F v_k = \begin{pmatrix} 0 \\ \tau_{lk} \\ u_m \tau_{mk} + \frac{\kappa}{(\gamma-1)Pr} \frac{\partial T}{\partial x_k} \end{pmatrix} \quad (2)$$

$$\tau_{lk} = \mu \left(\frac{\partial u_l}{\partial x_k} + \frac{\partial u_k}{\partial x_l} \right) - \frac{2}{3} \mu \frac{\partial u_n}{\partial x_n} \delta_{lk} \quad (3)$$

where subscripts k, l, m , and n take the values of 1, 2, and 3 denoting the body-fixed coordinates. All quantities are dimensionless. The working gas is air approximated by the calorically perfect gas model with a specific heat ratio of

$\gamma = 1.4$. The molecular viscosity μ is calculated using Sutherland's law. The thermal conductivity κ is obtained from $\kappa = \mu$, assuming that Prandtl number is constant with $Pr = 0.71$. For modeling turbulence, the molecular viscosity μ is replaced by $(\mu + \mu_t)$, where μ_t is the turbulent viscosity given by the turbulence model. Similarly, the thermal conductivity κ is replaced by $(\mu + \mu_t Pr / Pr_t)$, where the turbulent Prandtl number is $Pr_t = 0.90$. Reynolds number in Eq. (1a) is defined as shown in Eq. (4).

$$Re = \frac{\rho_\infty U_\infty L a_\infty}{\mu_\infty U_\infty} = \frac{Re_\infty}{M_\infty} \quad (4)$$

C. Computational methods

We used FAST Aerodynamic Routines (FaSTAR) [17], a high-speed flow solver developed at JAXA, for calculations. The system of equations (Eqs. (1) - (3)) was discretized and solved by cell-vertex finite volume method for unstructured grids with second-order accuracy in both space and time. We employed delayed detached-eddy simulation (DDES) [18] as the turbulence model in order to capture the wake turbulence accurately with a moderate computational cost. A numerical flux for the inviscid term was calculated by an advection upstream splitting method (AUSM) type scheme, simple low-dissipation AUSM (SLAU) [19]. The Green-Gauss method [20] was used for the gradient calculations within the monotone upstream-centered schemes for conservation laws (MUSCL) [21] framework along with Venkatakrishnan limiter [22]. For time integration, preconditioned lower-upper symmetric Gauss-Seidel scheme (p-LUSGS) [23] was adopted with the dual-time-stepping for unsteady simulations. Here, the time step was set to $dt \approx 8.8 \times 10^{-6}$ sec and the inner iteration number was 5.

In addition to the DDES simulations, the corresponding inviscid simulations are conducted for the purpose of comparison. In that case, Euler equations (Eq. (1b)) were solved instead of Navier-Stokes equations (Eq. (1a)).

D. Computational grids

We used MEGG3D [24], an automatic meshing tool developed at JAXA, to generate the computational grid shown in Fig. 5. As shown in this figure, the coordinate system was defined such that the X-axis was along the axial direction of the vehicle, the Y-axis was the axis around which the pitch moment was defined, and the Z-axis was orthogonal to these two. It was known that the behavior of the boundary layer at the Nose greatly affected the wake of slender bodies [25]. Thus, we needed to generate grids whose first cell height was small enough to accurately resolve the boundary layer. Unfortunately, however, boundary layers at the Nose are generally too thin to capture completely. Thus, in this

study, we set the first cell height such that $y^+ < 0.1$, aiming to predict the boundary layer at the Nose as accurately as possible, with reasonable computational cost. The resulting number of computational nodes was approximately 31.77 million. This grid was labeled as the “medium” grid. The “coarse” and “fine” grids were obtained by decreasing/increasing the grid space in each direction by a factor of $\sqrt[3]{3}$, resulting in 19.71 million and 49.70 million node grids, respectively. A grid dependency study was conducted using these three grids for an AOA of 60 degrees. Here, we select 60 degrees as the representative angle since at this angle, small vortices are generated in the wake of the vehicle, and the pitching moment coefficient is highly dependent on the grid density. Table 1 shows that the pitching moment coefficient is converged at the “medium” grid, and therefore, we use this grid in this study.

E. Computational conditions

The computational conditions were selected to correspond to wind-tunnel tests [15, 16]. The freestream flow velocity U_∞ was set to 30 m/s (Mach number $M_\infty = 0.08643$). The freestream Reynolds number based on the body length L was $Re_\infty = 6.0 \times 10^5$. The center of gravity was set to 65 percent of the body length from the Nose tip.

For convenience, we classified the computational cases according to AOA as in shown Table. 2. We calculated 18 cases in total; nine cases for AOAs less than 90 degrees and nine cases for AOAs greater than 90 degrees.

F. Aerodynamic coefficients

The pitching moment coefficient is defined as follows.

$$C_m = \frac{M_y}{q_\infty S_{base} L} \quad (5)$$

The pitching moment M_y is determined from $\sum_i \{F_{zi}(x_G - x_i) - F_{xi}(z_G - z_i)\}$, where x_G and z_G are the X and Z coordinates of the center of gravity, respectively. F_{xi} and F_{zi} are calculated from pressure and friction forces.

G. Data processing

All the results in this paper represent time-averaged values. For the time-averaging process, data were obtained at every 100 steps, from step 20100 to step 40000, yielding a total of 200 data points. These values were established such that this process included at least ten cycles, and each cycle included at least ten instantaneous values. Here, a cycle was defined as the main period of the pitching moment hysteresis calculated using a Fast Fourier Transform (FFT).

As an example, we select 60 degrees of AOA, and show the time history of the pitching moment coefficient and the

results of FFT in Figs. 6 and 7, respectively. From Figs. 6 and 7, it is found that the main period of the C_m hysteresis is approximately 1400 steps.

III. Results and discussion

A. Validation

Figure 8 shows the comparison of the DDES results, the inviscid simulation results, and experimental data [16] for the pitching moment coefficients. A positive pitching moment represents a nose-up moment, and a negative pitching moment corresponds to a nose-down moment. As shown in Fig. 8, the results of our calculations agree well with those of experiment. We argue that this is because we selected DDES model as the turbulence model to capture the wake, which had not been accurately resolved by RANS models (see Appendix B). Bhagwandin [26] reports that nearly equal pitching moments can be obtained between numerical simulations and experiments, even though there a sting is present in the downstream of experimental models. This is because, unlike their influence on axial forces, the influence of a sting on pitching moments is small [26]. Similarly, we argue that the presence of a sting in the reference experiment [16] hardly affects pitching moment coefficients, and thus, we consider our calculation results to be valid. Additionally, as shown in Fig. 8, the pitching moment coefficients of the inviscid calculation take the form of a sinusoidal curve; the present body configuration is designed to have such characteristics, however, this has obviously been affected by viscosity and turbulence as evident in DDES profile. Therefore, comparing the DDES results with the inviscid results aids in explaining why pitching moment coefficients exhibit this complicated, non-linear distribution represented in Fig. 8. Refer to Sec. III. B for further discussion.

B. Relation between flowfield and pitching moment

Since the difference in the pitching moment coefficient between DDES and the inviscid simulation is relatively large at 10 to 60 degrees and 120 to 170degrees of AOA (Fig. 8), for brevity we will focus only on the following angles: we have selected 20, 40, and 60 degrees of AOA as representative cases for the range of 20-60 degrees and 130, 150, and 170 degrees for that of 120-170 degrees.

1) Forward angles ($0 < \text{AOA} \leq 90 \text{ deg.}$)

- 20 deg. AOA

Firstly, we will discuss on the case of 20 degrees AOA. Figure 9 (a) shows the isosurface of the second invariants of the velocity gradient tensor (Q) colored with the pressure coefficient ($Q = 5 \times 10^{-7}$). Here, Q is obtained from $Q = (|\Omega|^2 - |S|^2)/2$, and the velocity component used in this equation is nondimensionalized by the freestream speed of sound. From Fig. 9 (a), we can observe a pair of vortices generated from the Nose, and another pair of vortices formed at the aftbody. To illustrate the structure of these vortices in more detail, we show 2D velocity vectors colored with x -vorticity magnitude for $x/L = 0.36, 0.50$, and 0.70 cross-sections in Fig. 9 (b). Here, in Fig. 9 (b), the body surface is colored with the pressure coefficient. It can be seen in Fig. 9 (b) that the vortex-pair generated from the Nose and the other pair formed from the aftbody are rotating in the same direction; therefore, the vortex-pair generated from the aftbody are not secondary vortices of those generated from the Nose. For convenience, in this study, we will call the vortices produced from the Nose at forward AOAs “V1”, and ones generated from the aftbody “V2.” Moreover, we find that V1 and V2 cause a pressure decrease on the body surface as shown in Fig. 9 (b). V1 decreases the on-surface pressure at the forebody ($x/L < 0.50$). However, at the aftbody ($x/L > 0.50$), the pressure decrease due to V1 is hardly observable since V1 detaches from the body surface. Instead, the decrease of the pressure due to V2 is dominant, as V2 does not detach from the body but rather continues near the body surface. Figure 10 compares the pressure coefficients both on the body surface and on the symmetry plane, between the DDES and inviscid calculations. In Fig. 10 (a), the pressure decrease is visible between the vicinity of the center of gravity ($x/L = 0.65$, designated by the red circle) and the near-Base on the leeward side. This pressure decrease is, as mentioned above, apparently due to V2. In addition, the pressure decreases also in the wake of the Base. This appears to be caused by wake-vortices. V1 is also considered to decrease the on-surface pressure near the Nose. However, the pressure decrease due to V1 is small; hence its effect on the pressure distribution cannot be observed in Fig. 10 (a). On the other hand, these vortices are not generated in the case of inviscid calculation, and such a decrease in pressure does not occur, as shown in Fig. 10 (b). Instead, a pressure decrease due to flow expansion is visible near the edges of the Base especially on the windward side, and the pressure increases on the leeward side due to stagnation.

As shown in Fig. 11, these pressure differences between the windward side and the leeward side generates (local) normal force (C_N) [27]. On the aftbody ($x/L > 0.50$) where noticeable pressure differences between DDES and inviscid calculations are produced, positive normal forces near the Base arise in the case of DDES, whereas negative ones are generated in the inviscid case. This difference is due to the different pressure distribution between the DDES and the inviscid calculations (Fig. 10). The pressure decrease on the leeward side is generated due to V2 in the case of DDES,

however in the case of inviscid calculation, the pressure decreases due to expansion on the windward side and increases due to stagnation on the leeward side.

Similarly, the local pitching moment distributions in Fig. 12 are obtained by multiplying the distance from the center of the gravity with the normal forces shown in Fig. 11. In Fig. 11, the difference in the normal force distributions between DDES and inviscid calculations is hardly observable near the Nose. However, in Fig. 12, the difference between the local pitching moments is clear between these two cases. Around the center of gravity where the difference in the normal forces have been generated, the local pitching moments take almost the same values ($C_m \approx 0$). This is because pitching moments are expressed as (force) \times (distance from the gravity center). In the case of DDES, the pitching moment is slightly larger near the Nose in comparison to the inviscid case. This is because the pressure decrease due to V1 results in the slightly greater normal forces. On the other hand, near the Base ($x/L > 0.8$), a significant difference in the pitching moment distributions between the DDES and inviscid calculations is generated; a nose-up (positive) moment acts in the case of DDES, while a nose-down (negative) moment arises in the case of DDES. As in Fig. 11, this is because positive and negative normal forces are generated in the DDES and inviscid calculations, respectively, near the Base (being in mind that positive normal forces aft of the center of gravity creates a negative pitching moment). In short, it is found that at an AOA of 20 degrees, vortices V1 and V2 are generated, and each vortex-pair affects the pitching moment; V1 generates a nose-up moment at the Nose and V2 causes a nose-down moment at the aftbody. In this case, V2 has the greater effect on the on-surface pressure distribution, resulting in a smaller pitching moment coefficient for DDES (DDES: $C_m = 0.12$, inviscid: $C_m = 0.28$).

The above-mentioned relationship between the local normal force and the local pitching moment also applies to other AOAs. Thus, for brevity, we will focus only on the local pitching moment.

- 40 deg. AOA

As with the 20 degrees AOA case, the Q isosurface at 40 degrees AOA is shown in Fig. 13 ($Q = 5 \times 10^{-7}$). It can be seen in Fig. 13 that V1 and V2 are generated from the Nose and from $x/L \approx 0.50$, respectively. Since the flowfield at 40 degrees is asymmetrical and complex, it is difficult to determine a detailed flow structure from Fig. 13 alone. Thus, the 2D velocity vectors on the $x/L = 0.17, 0.36, 0.50, 0.70, 0.80,$ and 0.90 cross-sections seen from the body-axis direction are shown in Fig. 14. According to Fig. 14, V1 is generated at $x/L = 0.18$ and 0.36 (Nose). Here, V1 is symmetrical at $x/L = 0.18$, but exhibits a small amount of asymmetry at $x/L = 0.36$. Then, at $x/L = 0.50$, V2 is formed outside V1, and V1 begins to detach from the body. In addition, V2 is symmetrical, whereas V1 is asymmetrical. At

$x/L=0.70$, V1 **detaches** further from the body, and the asymmetry of V1 and V2 is notable. At $x/L=0.80$, on the +Y side, V1 and V2 **appear to** combine, and these vortices are already merged at $x/L=0.90$. In this study, we define this vortex as “V1+V2”. On the other hand, on the -Y side, V1 and V2 are not **merged**. Furthermore, V1 detaches from the body and weakens from $x/L= 0.70$ to 0.90 .

Figure 15 shows 2D velocity vectors and the on-surface pressure for $x/L=0.36$, 0.50 , and 0.70 cross-sections (Fig.15 (a): +Y side only; Fig.15 (b)b; -Y side only). The effect of the vortices on the on-surface pressure distribution is **illustrated in** Fig. 15. At the forebody ($x/L<0.50$), V1 causes a pressure **decrease** on the body surface, yet at the aftbody ($x/L>0.50$), **V2, not V1, acts to decrease** the on-surface pressure; V1 **detaches** from the body at $x/L\approx 0.50$, and instead, the new vortex V2 is generated. Moreover, V1+V2 **forming** on the +Y side is also **considered to be a** cause of pressure reduction, as shown in Fig.15.

Figure 16 shows the pressure distributions obtained from both DDES and inviscid calculation. From Fig. 16 (a), in the case of DDES, the pressure **decreases** on the Nose part and the aftbody due to V1 and V2, respectively. The pressure **decrease** also occurs in the wake of the Base. Meanwhile, in Fig. 16 (b), in the inviscid case, the pressure **increases on** the downstream side of the vehicle **due to** the stagnation, especially **aft of** the Base. Furthermore, the pressure **decreases** due to expansion at the edges of the Base, as with the 20 degrees AOA case.

The local pitching moment distributions **are shown** in Fig. 17. In Fig. 17, unlike **the 20 degrees AOA case, a significant** difference in the pitching moment distribution between **the** DDES and inviscid calculation is observed both forward and **aft** of the center of gravity. Forward of the center of gravity ($x/L<0.65$), a larger nose-up moment is generated in DDES compared with the inviscid case. In this region, both V1 and V2 exist, but considering the fact that the difference between DDES and inviscid calculation is **particularly apparent** at $x/L<0.5$ where V1 has the notable effect on the on-surface pressure, we can say that V1 contributes **more** to this nose-up moment **in comparison to** V2. **Aft** of the center of gravity ($x/L>0.65$), a nose-down moment acts near the Base in the case of DDES, whereas a nose-up moment is generated in the case of Inviscid calculation. This difference arises due to the different flowfields between **the** inviscid calculation and DDES; stagnation **occurs in the** inviscid calculation, **whereas** V2 and V1+V2 are formed in DDES. Accordingly, V1, V2 and V1+V2 cause a pressure **decrease** on the leeward side, and **together** these **effects** result in the disparity in the pitching moment coefficients between DDES and the inviscid case at this AOA (DDES: $C_m = 0.23$ inviscid: $C_m = 0.42$).

- 60 deg. AOA

Furthermore, the case of 60 degrees AOA will be discussed. As with the other forward angles, the Q isosurface is shown in Fig. 18 ($Q = 5 \times 10^{-7}$). From Fig. 18, it can be seen that the flowfield is asymmetric as well as at an AOA of 40 degrees. In addition, V1 is produced from the Nose, and detaches from the body as it flows downstream. Since it is difficult to determine a detailed flow structure from Fig. 18 alone, the 2D velocity vectors on the $x/L=0.17, 0.36, 0.43, 0.50, 0.70,$ and 0.90 cross-sections seen from the body-axis direction are shown in Fig. 19. For $x/L \leq 0.50$, the vortex structure is similar to that of the 40 degrees AOA case; however, it becomes less clear downstream.

Firstly, at $x/L=0.17$ and 0.36 , the generation of V1 is observed. Here, the flowfield begins to become asymmetric at $x/L=0.36$. Next, at $x/L=0.43$, on the +Y side, V2 is formed outside V1. Meanwhile, on the -Y side, V2 does not form, but V1 begins detaching from the body. V1 and V2 formed on the +Y side are likely to merge at $x/L=0.50$, and V1+V2 is already generated at $x/L=0.70$. It can be seen on the -Y side that V1 detaches from the body as it streams from $x/L=0.43$ to the leeward side. Moreover, V1+V2 also detaches from the body as it proceeds to the downstream. At $x/L=0.90$, weak vortices (V1+V2 on the +Y side, V1 on the -Y side) are formed in the region away from the vehicle. On the -Y side of $x/L=0.90$, the new vortex V2 is generated. Here, because the vorticity magnitude of V2 is relatively small, V2 is considered weak.

The effect of these vortices on the pressure distribution is depicted in Fig. 20. Figure 20 shows that V1 causes a pressure decrease at the forebody, yet this effect becomes small at the aftbody since V1 detaches from the body as it flows downstream. Moreover, the decrease in pressure near the Base is not significant because V1, V2, and V1+V2 are weak vortices, and V1 and V1+V2 are formed away from the body, as shown in Fig.19.

Figure 21 shows the pressure coefficients acquired from the DDES and inviscid calculations. In Fig. 21 (b), in the case of the inviscid calculation, the pressure increases in the downstream of the vehicle due to the stagnation. On the other hand, in the DDES case (Fig. 21 (a)), the pressure on the leeward side decrease due to the vortices (V1, V2, and V1+V2). Specifically, at the Nose part, the on-surface pressure is greatly decreased since there exists V1. The pressure decrease at the aftbody is smaller than that at the forebody because V1 has already detached from the body in this region and V2, which forms near the Base, is a weak vortex.

The local pitching moment distributions for both the DDES and inviscid calculations are shown in Fig. 22. As Fig. 22 indicates, a significant difference in pitching moment distributions arises both forward and aft of the center of gravity. Forward of the center of gravity ($x/L < 0.65$), the pitching moment from DDES is greater than that of the inviscid calculation. This is because V1 generates a pressure decrease on the downstream side in the case of DDES,

whereas stagnation increases the pressure in the case of the inviscid calculation. Aft of the center of gravity ($x/L > 0.65$), a nose-down (negative) moment is generated in the case of DDES, while a nose-up (positive) moment acts near the Base in the inviscid case. As with the region forward of the center of gravity, stagnation generated in the case of the inviscid calculation and the vortices (V2 and V1+V2) formed in the DDES case cause this difference in the pitching moment distributions. As a result, the local pitching moments in the DDES case are greater forward of the center of gravity due to the effects of V1, but aft of the center of gravity, these moments are smaller due to V2 and V1+V2. Considering the entire vehicle, these differences in the pitching moment coefficients cancel each other out, and consequently, the pitching moment coefficients of the DDES and inviscid cases take almost the same value (DDES: $C_m = 0.39$, inviscid: $C_m = 0.37$).

The results at forward angles are summarized here. At forward angles, vortices V1 and V2 are generated from the Nose and aftbody, respectively. At AOA of 40 and 60 degrees, V1 and V2 merge, and a new vortex V1+V2 is produced only on the +Y side, leading to flow asymmetry. From the comparison between the DDES and inviscid calculations, these vortices are found to decrease the pressure on the leeward side in the DDES case, causing the differences in the pitching moment coefficients in comparison to the inviscid calculation.

2) Backward angles (90 deg. < AOA < 180 deg.)

- 130 deg. AOA

Firstly, we discuss the results at an AOA of 130 degrees. Figure 23 shows the Q isosurface colored with the pressure coefficient ($Q = 5 \times 10^{-7}$). It can be seen from Fig. 23 that a group of vortices is generated near the Base. For convenience, we define these vortices as “V3” in this paper. In addition, a longitudinal vortex (designated as “V4” hereafter) is formed from the vicinity of the center of gravity. No large vortex structures are observed in the vicinity of the Nose, yet a group of vortices (called “V5”) is produced.

In order to explain the effect of these vortices on the on-surface pressure distribution, the pressure coefficients both on the body surface and on the symmetry plane are shown in Fig. 24 (a). For comparison, the pressure coefficients obtained from the inviscid calculation are also shown in Fig. 24 (b). As shown in Fig. 24 (a), the pressure decreases significantly due to V3 and V4 from the near-Base to the vicinity of the center of gravity. A pressure decrease also occurs at the Nose, caused by V5. As shown in Fig. 24 (b), in the inviscid case, on the leeward side, the pressure decrease due to expansion is visible at the edges of the Base, yet the pressure increases in the other regions due to stagnation.

Figure 25 shows the local pitching moment distributions. As shown in Fig. 25, the significant difference in the pitching moment distributions between the DDES and Inviscid calculations arises both forward and aft of the center of gravity ($x/L=0.65$). Forward of the center of gravity ($x/L<0.65$), a nose-up moment acts in the case of DDES, whereas a nose-down moment is generated in the inviscid case. This is because, on the leeward side, the pressure increases due to stagnation in the case of inviscid calculation, whereas the pressure decreases because of V4 and V5 in the case of DDES, as shown in Fig. 24. Aft of the center of gravity ($x/L>0.65$), a nose-down moment acts in both DDES and Inviscid calculation. In the Inviscid case, the large nose-down moment acts near the Base, because of the pressure decrease at the edges of the Base. In the case of DDES, a nose-down moment arises between the vicinity of the center of the gravity and the Base ($x/L > 0.65$). This is due to the decrease in the pressure caused by V3 and V4. These positive (in the forward section) and negative (in the aft section) moments cancel each other out in the case of DDES, whereas in the inviscid case, only a negative moment is generated. Therefore, a large difference in the pitching moment coefficients between DDES and inviscid calculation is apparent (see Fig. 8, DDES: $C_m = -0.19$, inviscid: $C_m = -0.43$).

- 150 deg. AOA

For the case of 150 degrees AOA, the Q isosurface is shown in Fig. 26 ($Q = 5 \times 10^{-7}$). According to Fig. 26, V3 is generated near the Base and V4 forms from the vicinity of the center of gravity. The pressure coefficients obtained from the DDES and inviscid calculations are shown in Fig.27. As shown in Fig. 27 (a), in the case of DDES, the pressure decreases between the Base and the vicinity of the center of gravity due to V3 and V4. On the other hand, in the inviscid case (Fig. 27 (b)), stagnation causes a pressure increase specifically at the Nose on the leeward side. Also, it can be seen that the pressure decreases at the edges of the Base due to expansion on the downstream side.

The local pitching moment distributions are shown in Fig. 28. We will investigate the influence of these differences in flowfields on the pitching moments. As shown in Fig. 28, the difference in the pitching moment distributions between the DDES and inviscid calculations arises both forward and aft of the center of gravity. Forward of the center of gravity ($x/L<0.65$), a nose-up moment acts in the case of DDES, but a nose-down moment is produced in the case of the inviscid calculation. As shown in Fig. 27, this is due to the fact that on the leeward side the pressure decreases due to V4 in the case of DDES, whereas stagnation causes an increase in pressure in the inviscid case. Here, in the case of DDES, a pitching moment is barely generated at the Nose as V5 does not form unlike in the case of 130 degrees AOA. Aft of the center of gravity ($x/L>0.65$), a nose-down moment acts in both cases. In the case of inviscid

calculation, a large nose-down moment acts near the Base due to the pressure decrease at the edges of the Base. In the case of DDES, in contrast, the pressure decrease caused by V3 and V4 generates a nose-down moment in the vicinity of the center of the gravity and the Base. Therefore, as with the 130 degrees AOA, in the case of DDES, these positive and negative moments cancel each other out. Meanwhile, in the inviscid case, a negative moment is generated both forward and aft of the center of gravity, and thus, a significant difference in the pitching moment coefficients between the DDES and inviscid calculations is apparent (DDES: $C_m = -0.10$, inviscid: $C_m = -0.37$).

- 170 deg. AOA

Finally, we will discuss the case of 170 degrees AOA. Figure 29 shows the Q isosurface colored with the pressure coefficient ($Q = 5 \times 10^{-7}$). As shown in Fig.29, the Base is surrounded by a “jellyfish shaped” vortex. For convenience, in this study, we define the leeward side of this vortex as “V3” and the windward as “V3’”. In addition, V5 is produced at the Nose. Figure 30 shows the pressure distributions obtained from both DDES and inviscid calculations. As shown in Fig. 30 (a), V3 and V3’ cause a pressure decrease on the leeward and windward sides of the near-Base region, respectively. In the vicinity of the Nose, a decrease in pressure due to V5 is barely observed, and therefore, V5 is considered a weak vortex. In the case of the inviscid calculation, from Fig. 30 (b), the stagnation region appears to be limited to the area around the Nose tip only. Along the edges of the Base, the pressure decreases due to expansion in agreement with other backward angle cases. Comparing Figs. 30 (a) and (b), the obvious difference in the pressure distributions between the DDES and inviscid calculations can be observed only near the Base where V3 and V3’ exist.

The local pitching moment distributions are shown in Fig. 31. As shown in Fig. 31, forward of the center of gravity ($x/L < 0.65$), a nose-down moment acts in both the DDES and inviscid calculations, and the difference in pitching moment distributions between these two cases is barely visible. However, in the vicinity of the Nose, a slightly greater (negative) pitching moment arises in the case of the inviscid calculation because of the pressure increase due to stagnation. Aft of the center of gravity ($x/L > 0.65$), the pitching moment distribution in the case of DDES is completely different from the other backward angles; both nose-up and nose-down moments are produced. The nose-up moment is generated at $x/L > 0.90$ since the pressure decrease due to V3’ is greater than that of V3. Just forward of that region ($0.72 < x/L < 0.90$), a nose-down moment is produced because of the greater pressure decrease on the leeward side (Fig. 30 (a)). In the inviscid case, as with the other backward angles, a nose-down moment arises aft of the center of gravity. In the case of DDES the nose-up moment forward of the center of gravity and the nose-down moment aft of the center

of gravity cancel each other out, resulting in a small net pitching moment value. On the other hand, in the inviscid case, since only nose-down moments act both forward and aft of the center of gravity, the absolute value of the pitching moment coefficient for the inviscid calculation becomes slightly larger than that of DDES, as shown Fig. 8 (DDES: $C_m = -0.05$, inviscid: $C_m = -0.15$).

We summarize backward angles as follows. A group of vortices V3 is generated and affects the pitching moment distribution near the Base; it causes a decrease in pitching moments at 130 and 150 degrees. At 170 degrees, V3' arises on the windward side of the Base and increases the pitching moment. Depending on the angles, vortices V4 and/or V5 are produced and have a certain effect on local pitching moments.

IV. Conclusions

In this study, we numerically calculated the flow around a *slender-bodied* reusable rocket at high angles of attack (which mimics its turnover maneuver under a quasi-static-process assumption) between 0 and 180 degrees, and investigated the aerodynamic coefficients and the flowfields. According to our results,

- Our calculation agreed well with those of the corresponding experiments in terms of the pitching moment coefficient by adopting DDES model as the turbulence model.
- We found that the pitching moment coefficients of inviscid calculations take the form of a sinusoidal curve, which is not seen in DDES; meaning the results of DDES are significantly impacted by the viscous and turbulence effects of the wake.
- We clarified the relationship between the flow structure and the aerodynamic characteristics by comparing the DDES and inviscid simulation results.
 - Two types of vortices are formed at forward angles; one is generated from the Nose and the other is produced from the aftbody. Especially at AOAs of 40 and 60 degrees, these vortices merge with each other, and flowfields become asymmetric. These vortices cause the pressure decrease on the leeward side of the vehicle and significantly affect the pitching moment.
 - Three types of vortices are generated at backward angles. A group of vortices affects pitching moment distributions near the Base. Vortices formed between the vicinity of the center of gravity and the Nose are responsible for the pitching moment variations depending on the angles.

We determined that pitching moment depends on complex flow phenomena, including five different vortex or bubble structures. This is a new discovery in this field.

Appendices

A. Information of Reference Experiments

The experiments [15, 16] were conducted at JAXA's planetary environment wind tunnel. The nozzle outlet diameter is 1.6 m with a turbulence level of less than 1%. The experimental conditions were the same as our calculations; the free stream flow velocity U_∞ was set to 30 m/s and the free stream Reynolds number based on the body length L was $Re_\infty = 6.0 \times 10^5$. The test model also corresponds to ours except for the sting installed at the Base at forward angles and at the Nose at backward angles, as shown in Fig. A1 (It was confirmed [15, 16] that the sting had very little influence on the pitching moment). A six-component balance was used to obtain aerodynamic forces and moments. The data were measured at 5 degrees AOA intervals between 0 and 180 degrees, with a sampling rate of 1000 Hz for 4000 instants. The pitching moment values are summarized in Fig. 8.

B. Results of RANS simulation

We conducted RANS simulations [28, 29] as well as DDES, and found that RANS cannot capture the wake accurately. The computational grid we used for RANS simulations was the same as DDES, and Spalart-Allmaras one-equation model without tripping (f_{t2}) term (SA-nof2) [28] was adopted as the turbulence model. Other computational methods and conditions corresponded to those of DDES. The pitching moment coefficients which were acquired from RANS simulations along with that of the experiment [16] and DDES are shown in Fig A2. The pitching moment coefficients from the RANS simulation deviate from that of the experiment significantly at AOAs of 40, 60, and 130 degrees, whereas those values show good agreement with that of the reference experiment [16] at the other AOAs. We select an AOA of 40 degrees as a representative angle and show the Q isosurface acquired from RANS simulation in Fig. A3. In Fig. A3, a pair of vortices V1 can be observed, yet the other pair of vortices V2 is not visible, unlike the DDES case shown in Fig. 13. In addition, as shown in Fig. A3, these vortices are symmetrical unlike in the DDES case (Fig. 15 (a)). From this result, we determined that DDES is more capable of predicting unsteady separated flow in comparison to a RANS simulation. Therefore, DDES would be ideal for use in this study.

Acknowledgments

These simulations described in this paper were performed on the JAXA Supercomputer System generation 2 (JSS2). We used FaSTAR as the fluid solver. We would like to thank Dr. Yasushi Ito for providing the meshing tool, MEGG3D. We appreciate the feedback offered by Dr. Taro Shimizu of Japan Aerospace Exploration Agency and Mr. Junya Aono of the Research Center of Computational Mechanics, Inc. We also would like to thank Mr. Yuji Shimojima of Tokyo University of Agriculture and Technology and Mr. Takuya Kinami of Yokohama National University for providing us with the experimental data, and Mr. Matthew Richardson of the University of Tokyo for proofreading our manuscript.

References

- [1] Inatani, Y., Naruo, Y., and Yonemoto, K., "Concept and Preliminary Flight Testing of a Fully Reusable Rocket Vehicle," *Journal of Spacecraft and Rockets*, Vol. 38, No. 1, 2001, pp. 36-42.
doi: 10.2514/2.3652
- [2] Pamadi, B. N., Neiryck, T. A., Hotcko, N. J., Scallion, W. I., Murphy, K. J., and Covell, P. F., "Simulation and Analysis of Stage Separation of Two-Stage Reusable Launch Vehicles," *Journal of Spacecraft and Rockets*, Vol. 44, No. 1, 2007, pp. 66-80.
doi: 10.2514/1.17896
- [3] Ridder, S. D., and Mooij, E., "Optimal Longitudinal Trajectories for Reusable Space Vehicles in the Terminal Area," *Journal of Spacecraft and Rockets*, Vol. 48, No. 4, 2011, pp. 642-653.
doi: 10.2514/1.51083
- [4] Dissel, A. F., Kothari, A. P., Livingston, J. W., and Lewis, M. J., "Weight Growth Study of Reusable Launch Vehicle Systems," *Journal of Spacecraft and Rockets*, Vol. 44, No. 3, 2007, pp. 640-648.
doi: 10.2514/1.26064
- [5] Manokaran, K., Vidya, G., Sivaramakrishnan, A. E., and Goyal, V. K., "Wing Planform Design optimization for Reusable Launch Vehicle," *Journal of Aircraft*, Vol. 46, No.2, 2009, pp. 726-730.
doi: 10.2514/1.39732

- [6] Nonaka, S., Ogawa, H., and Inatani, Y., "Aerodynamic Design Considerations in Vertical Landing Rocket Vehicle," 10th AIAA/NAL-NADA-ISAS International Space Planes and Hypersonic Systems and Technologies Conference, AIAA Paper 2001-1898, Kyoto, Japan, 2001.
doi: 10.2514/6.2001-1898
- [7] Nonaka, S., Imamura, Y., Shimotashiro, S., Ogawa, H., and Intani, Y., "Turnover Maneuver of Vertical Landing Rocket Vehicle," ISTS 2008, 2008-g-20, Hamamatsu, Shizuoka, Japan, 2008.
- [8] Kubota, H., Arai, I., and Matsuzaka, M., "Flat Spin of Slender Bodies at High Angles of Attack," *Journal of Spacecraft and Rockets*, Vol. 20, No. 2, 1983, pp. 108-114.
doi: 10.2514/3.28365
- [9] Kawamura, R. and Aihara, Y. (eds.), "Fluid Dynamics of High Angle of Attack," IUTAM Symposium Tokyo, Japan, September 13-17, 1992, Springer-Verlag, 1993.
doi: 10.1007/978-3-642-52460-8
- [10] Deng, X. Y., Tian, W., Ma, B. F., and Wang, Y. K., "Recent progress on the study of asymmetric vortex flow over slender bodies," *Acta Mechanica Sinica*, Vol. 24, Issue 5, 2008, pp. 475-487.
doi: 10.1007/s10409-008-0197-3
- [11] Jernell, L. S., "Aerodynamic Characteristics of Bodies of Revolution at Mach Numbers from 1.50 to 2.86 and Angles of Attack to 180°," NASA TM X-1658, 1968.
- [12] Jorgensen, L. H., "Prediction of Static Aerodynamic Characteristics for Space-Shuttle-Like and Other Bodies at Angles of Attack from 0° to 180°," NASA TN D-6996, 1973.
- [13] Kuzuu, K., Kitamura, K., Fujimoto, K., and Shima, E., "Numerical Flow Simulation of a Reusable Sounding Rocket during Turnover," 29th AIAA Applied Aerodynamics Conference, AIAA Paper 2011-3367, Honolulu, Hawaii, 2011.
doi: 10.2514/6.2011-3367
- [14] Kuzuu, K., Nonaka, S., Aono, J., and Shima, E., "Aerodynamic Characteristics and Kinematic Analysis during Turnover of a Reusable Sounding Rocket," 51st AIAA Aerospace Science Meeting including the New Horizons Forum and Aerospace Exposition, 2013-0802, Grapevine, Texas, 2013.
doi: 10.2514/6.2013-802

- [15] Shimojima, Y., “Study on Aerodynamic Characteristic of VTOL Rocket on Turn-Over Maneuver,” Graduation thesis, Tokyo University of Agriculture and Technology, Tokyo, Japan, 2016, (Japanese).
- [16] Kinami, T., “Aerodynamic Characteristics of Slender Bodies at Turnover,” Master’s thesis, Yokohama National University, Kanagawa, Japan, 2018, (Japanese).
- [17] Hashimoto, A., Murakami, K., Aoyama, T., Ishiko, K., Hishida, M., Sakashita, M., and Lahur, P., “Toward the Fastest Unstructured CFD Code “FaSTAR”,” 50th AIAA Aerospace Science Meeting including the New Horizons Forum and Exposition, AIAA Paper 2012-1075, Nashville, Tennessee, 2012.
doi: 10.2514/6.2012-1075
- [18] Spalart, P. R., Deck, S., Shur, M. L., Squires, K. D., Strelets, M. Kh., and Travin, A., “A New Version of Detached-Eddy Simulation, Resistant to Ambiguous Grid Densities,” *Theoretical and Computational Fluid Dynamics*, 20, 2006, pp. 181-195.
doi: 10.1007/s00162-006-0015-0
- [19] Shima, E., and Kitamura, K., “Parameter-Free Simple Low-Dissipation AUSM-Family Scheme for All Speeds,” *AIAA Journal*, Vol.49, No.8, 2011, pp.1963-1709.
doi: 10.2514/1.J050905
- [20] Mavriplis, D. J., “Revisiting the Least-Squares Procedure for Gradient Reconstruction on Unstructured Meshes,” 16th AIAA Computational Fluid Dynamics Conference, AIAA Paper 2003-3986, Orlando, Florida, 2003.
doi: 10.2514/6.2003-3986
- [21] Burg, C. O. E., “Higher Order Variable Extrapolation for Unstructured Finite Volume RANS Flow Solvers,” 17th AIAA Computational Fluid Dynamics Conference, AIAA Paper 2005-4999, Toronto, Ontario, Canada, 2005.
doi: 10.2514/6.2005-4999
- [22] Venkatakrishnan, V., “Convergence to Steady State Solutions of the Euler Equations on Unstructured Grids with Limiters,” *Journal of Computational Physics*, Vol. 118, Issue 1, 1995, pp. 120-130.
doi: 10.1006/jcph.1995.1084
- [23] Kitamura, K., Shima, E., Fujimoto, K., and Wang, Z. J., “Performance of Low-Dissipation Euler Fluxes and Preconditioned LU-SGS at Low Speeds,” *Communications in Computational Physics*, Vol. 10, No. 1, 2011, pp. 90-119.

doi: 10.4208/cicp.041109.160910a

- [24] Ito, Y. and Nakahashi, K., "Direct Surface Triangulation Using Stereolithography Data," *AIAA Journal*, Vol. 40, No. 3, 2002, pp. 490-496.

doi: 10.2514/2.1672

- [25] Keener, E. R., Chapman, G. T., Cohen, I., and Taleghani, J., "Side Forces on a Tangent Ogive Forebody with a Fineness Ratio of 3.5 at High Angles of Attack and Mach Numbers from 0.1 to 0.7," NASA TM X-3437, 1977.

- [26] Bhagwandin, V. A., "High-Alpha Prediction of Roll Dumping and Magnus Stability Coefficients for Finned Projectiles," *Journal of Spacecraft and Rockets*, Vol. 53, No. 4, 2016, pp.720-729.

doi: 10.2514/1.A33419

- [27] Kitamura, K., Nonaka, S., Kuzuu, K., Aono, J., Fujimoto, K., and Shima, E., "Numerical and Experimental Investigations of Epsilon Launch Vehicle Aerodynamics at Mach 1.5", *Journal of Spacecraft and Rockets*, Vol. 50, No. 4, 2013, pp. 896-916.

doi: 10.2514/1.A32284

- [28] Spalart, P. R., Allmaras, S., "A One-Equation Turbulence Model for Aerodynamic Flows," 30th Aerospace Sciences Meeting and Exhibit, AIAA paper 1992-439, Reno, Nevada, 1992.

doi: 10.2514/6.1992-439

- [29] Degani, D., and Schiff, L. B., "Computation of Turbulent Supersonic Flows Around Pointed Bodies Having Crossflow Separation," *Journal of Computational Physics*, Vol. 66, No. 1, 1986, pp. 173-196.

doi: 10.1016/0021-9991(86)90059-8

Figures

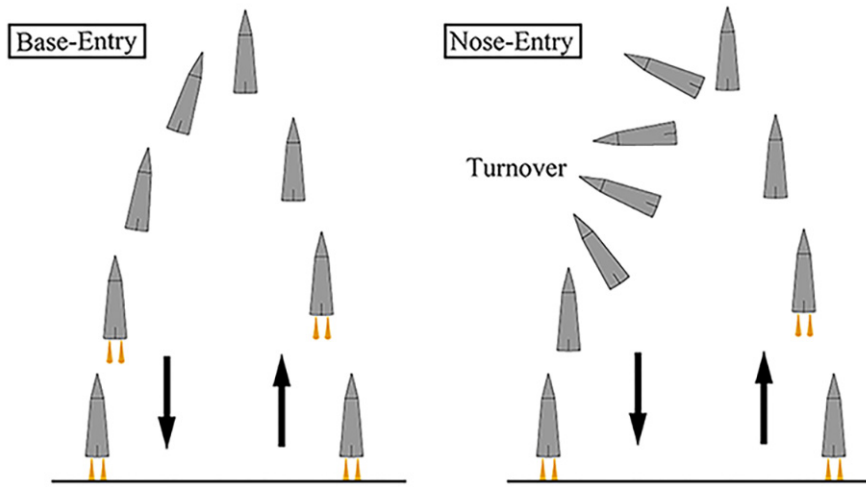


Fig. 1 Flight profile

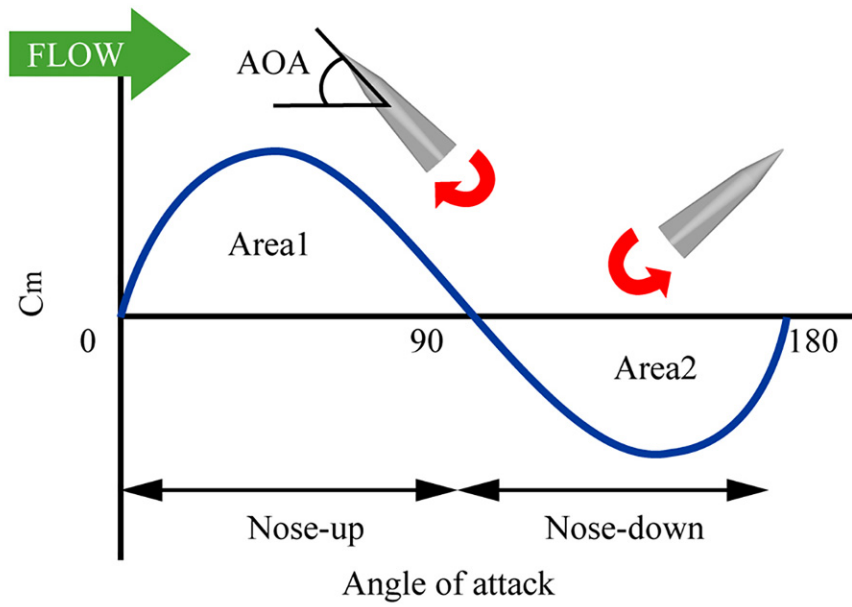


Fig. 2 Pitching moment characteristic of a slender body

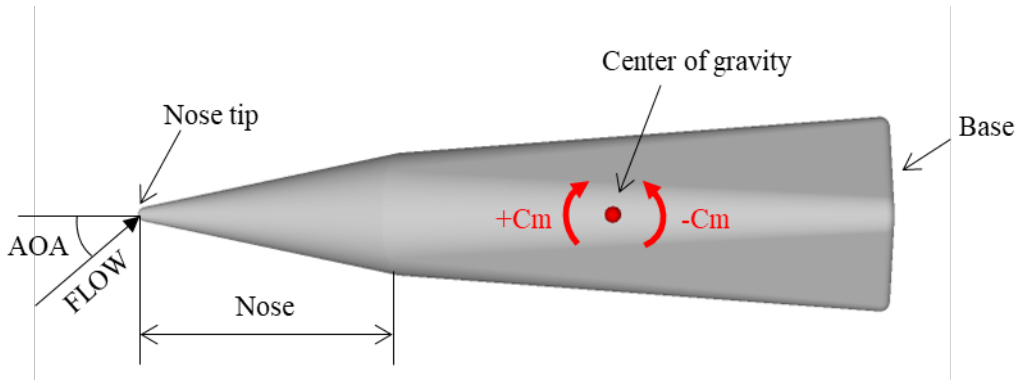
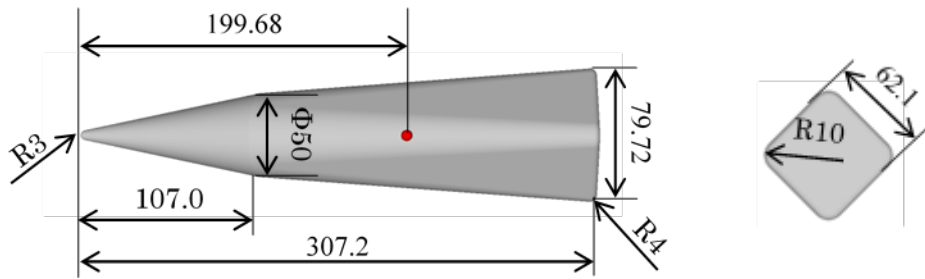


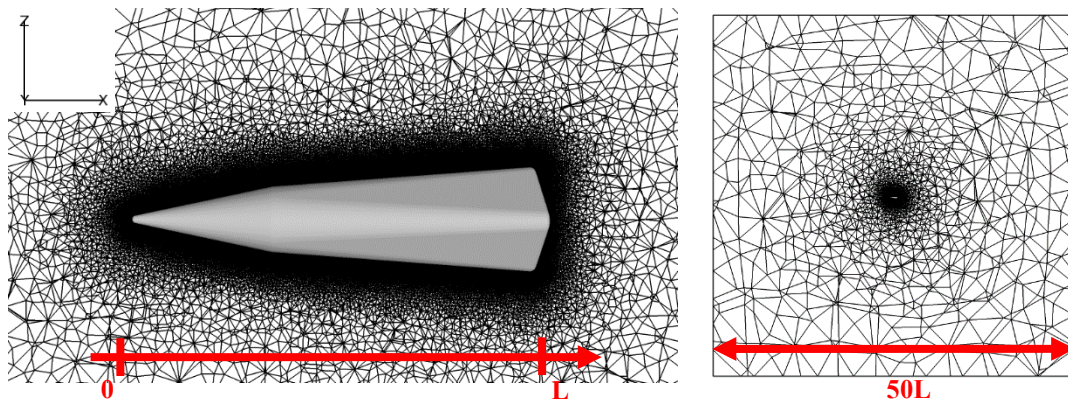
Fig. 3 Configuration and terms used in this paper



a) Side view

b) Base view

Fig. 4 Configuration (Side and Base views) [mm]



a) Body

b) Overview

Fig. 5 Computational grid

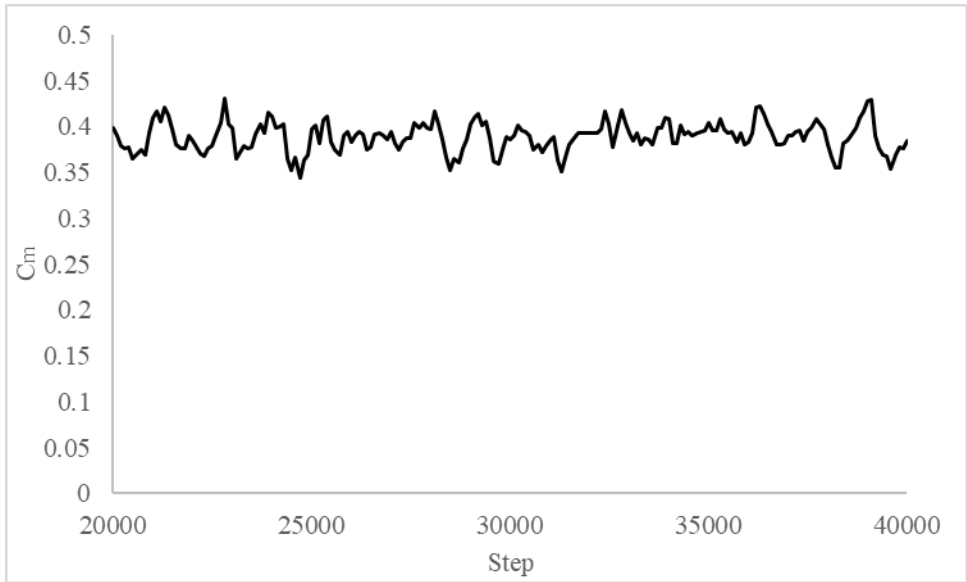


Fig. 6 Time history of pitching moment coefficient (AOA=60 degrees)

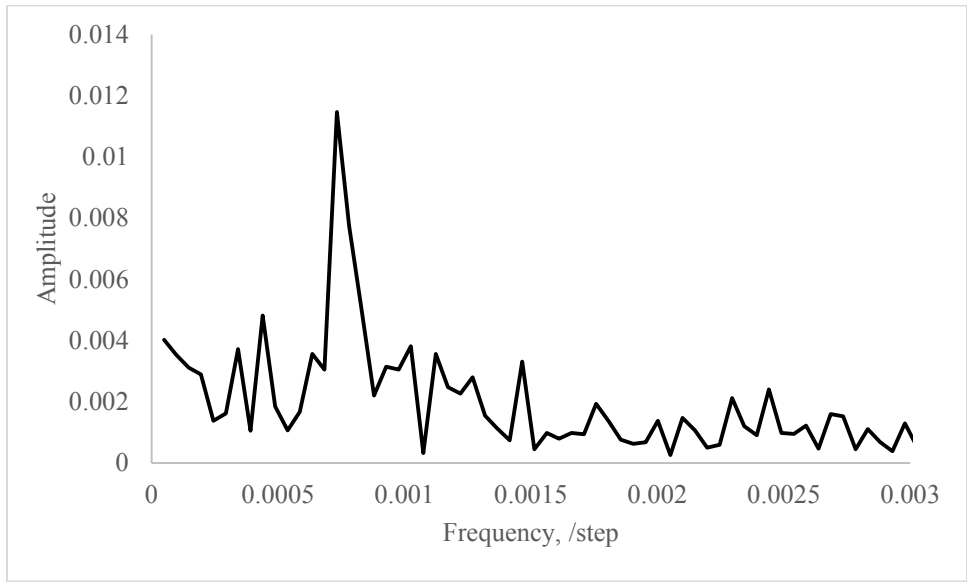


Fig. 7 FFT result (AOA=60 degrees)

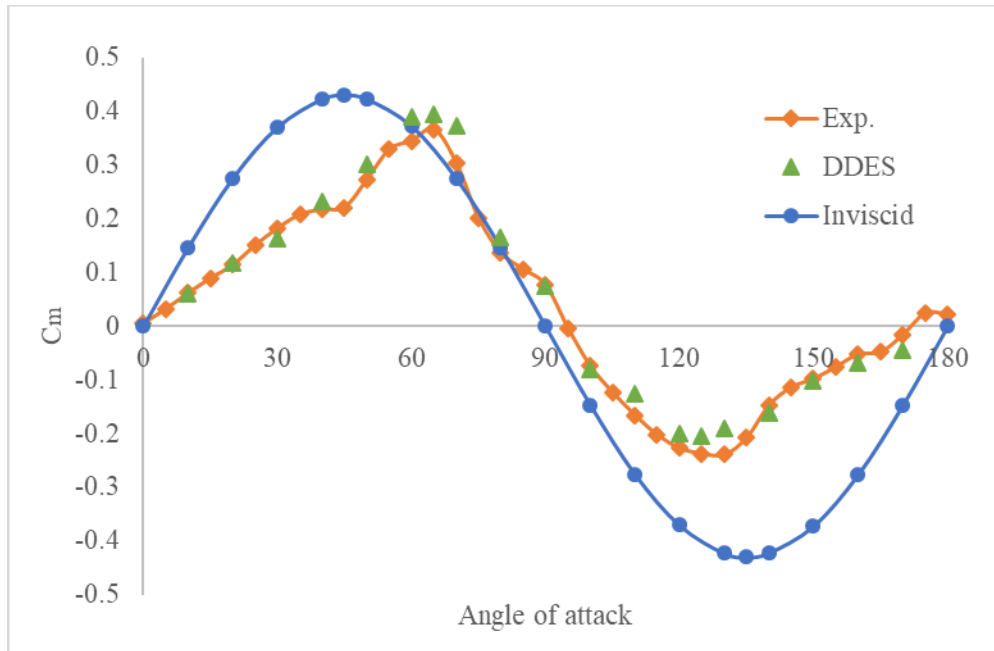


Fig. 8 Pitching moment coefficients

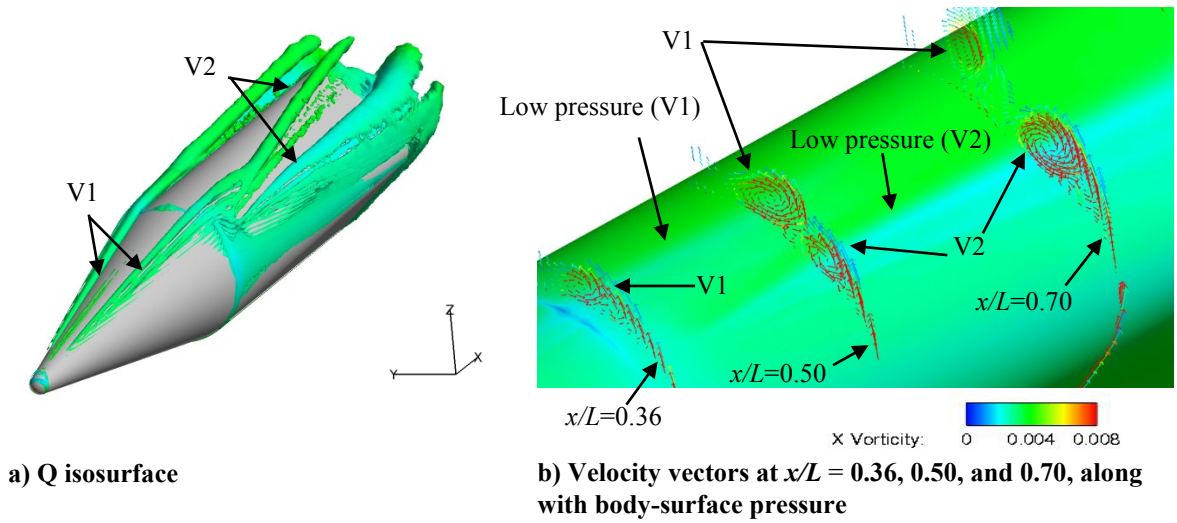


Fig. 9 Visualizations of vortices (AOA=20 degrees)

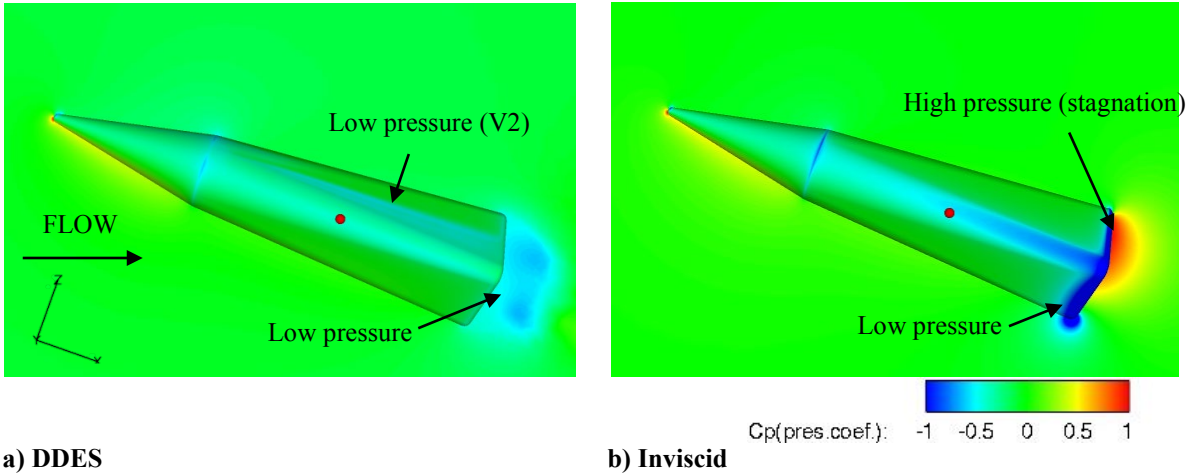


Fig. 10 Pressure distribution (AOA=20 degrees)

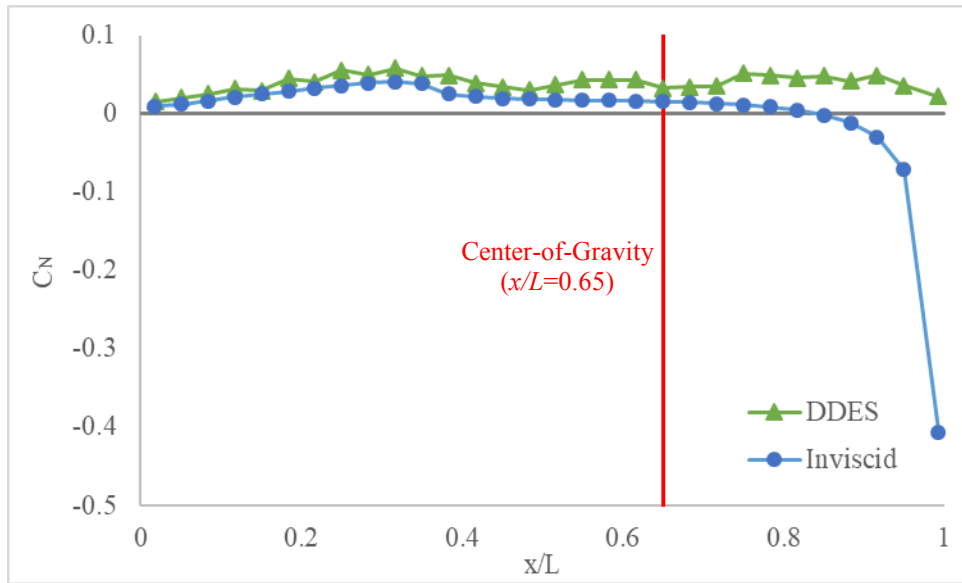


Fig. 11 Local normal force distributions (AOA=20 degrees)

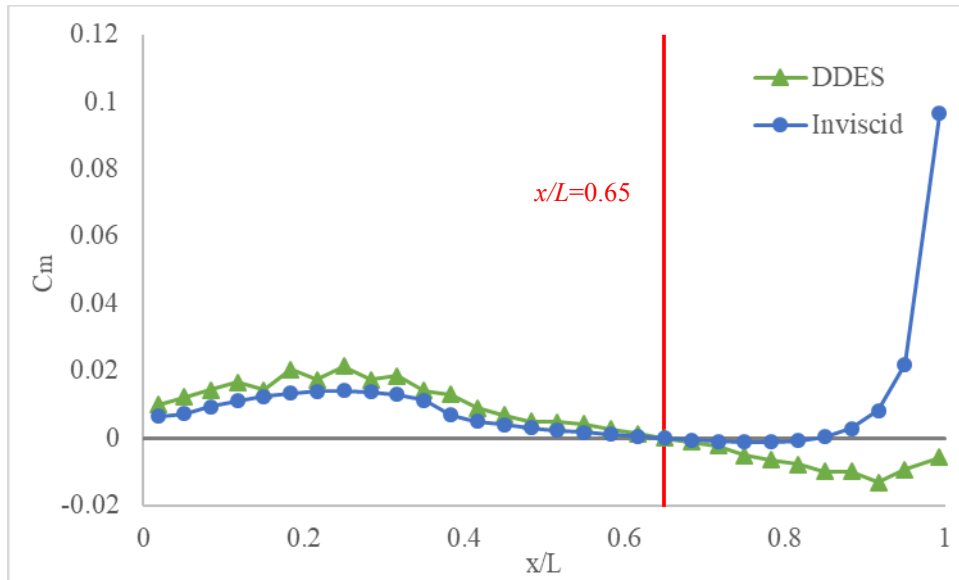


Fig. 12 Local pitching moment distributions (AOA=20 degrees)

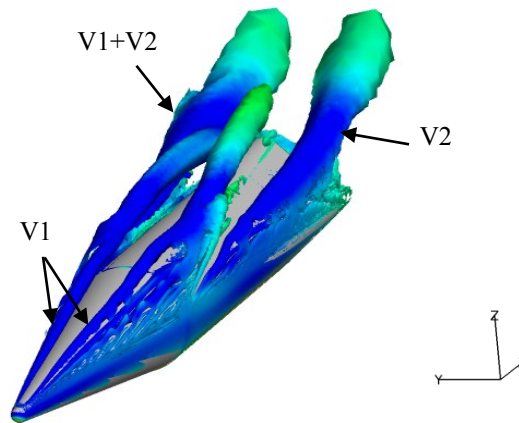
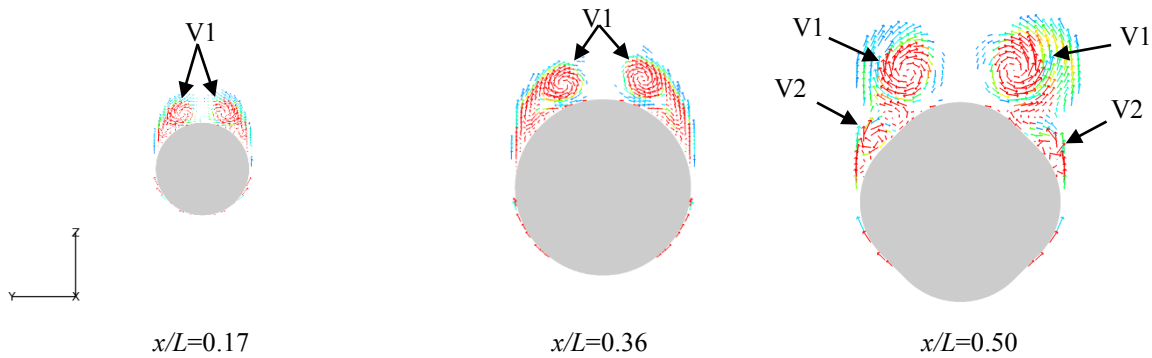


Fig. 13 Q isosurface (AOA=40 degrees)



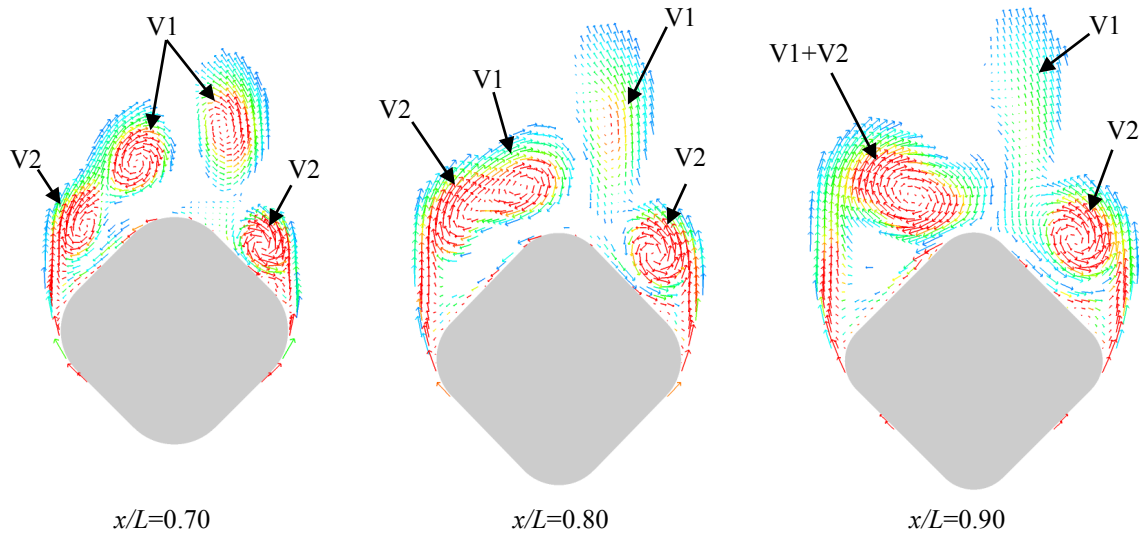


Fig. 14 2D velocity vectors colored with x-vorticity magnitude (AOA=40 degrees)

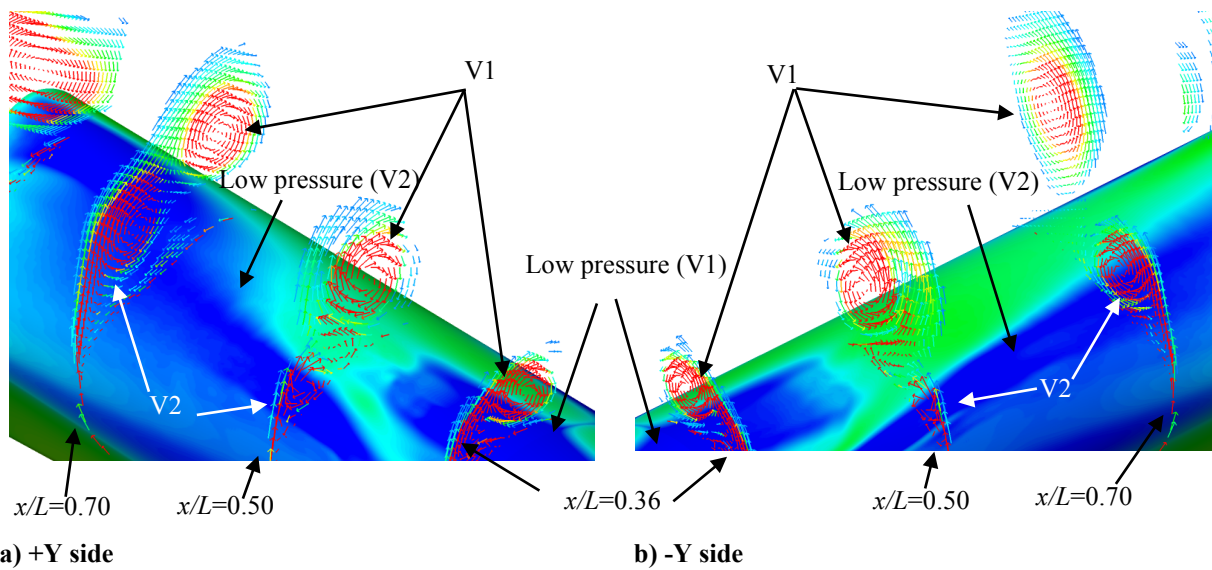
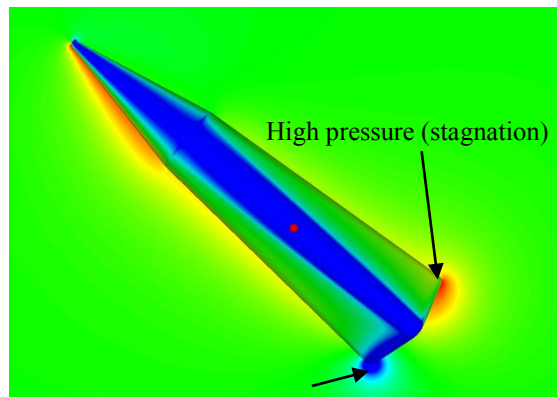
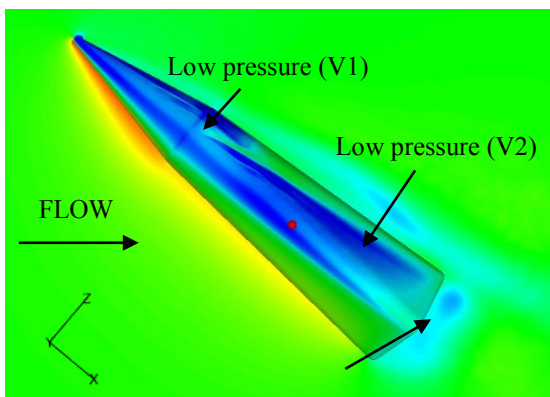
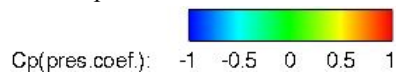


Fig. 15 Effect of vortices on surface pressure (AOA=40 degrees)



Low pressure

Low pressure



a) DDES

b) Inviscid

Fig. 16 Pressure distribution (AOA=40 degrees)

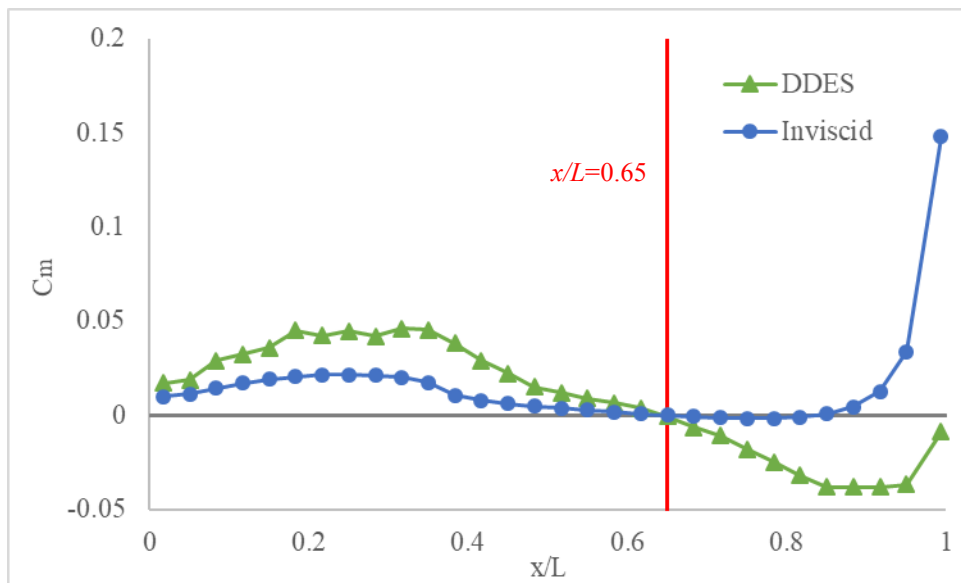


Fig. 17 Local pitching moment distribution (AOA=40 degrees)

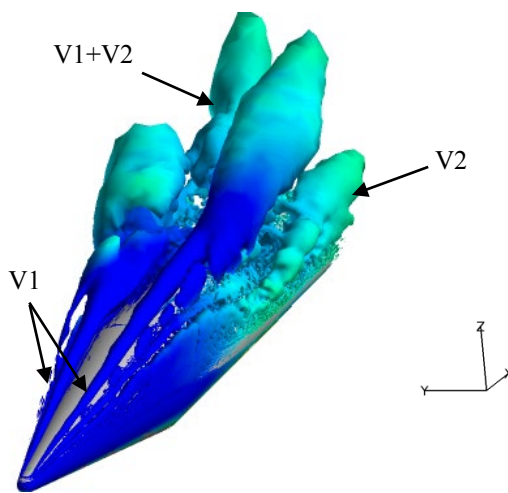


Fig. 18 Q isosurface (AOA=60 degrees)

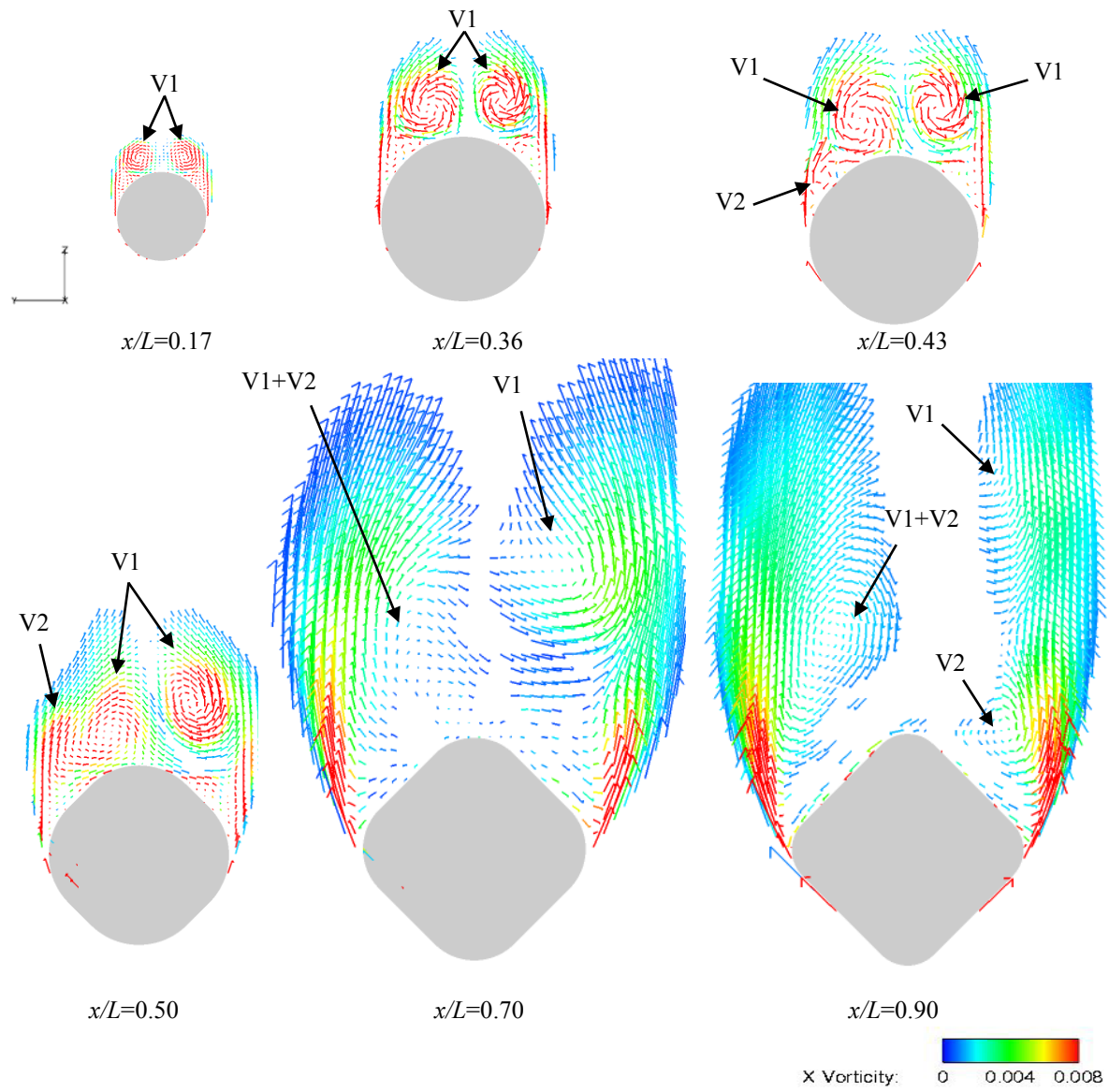


Fig. 19 2D vectors colored with X Vorticity magnitude (AOA=60 degrees)

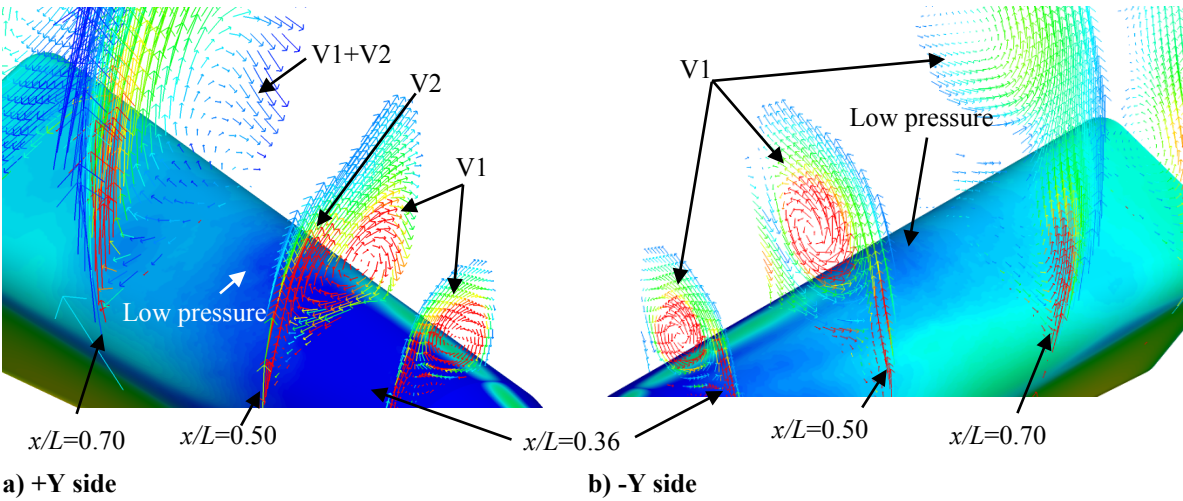


Fig. 20 Effect of vortices on surface pressure (AOA=60 degrees)

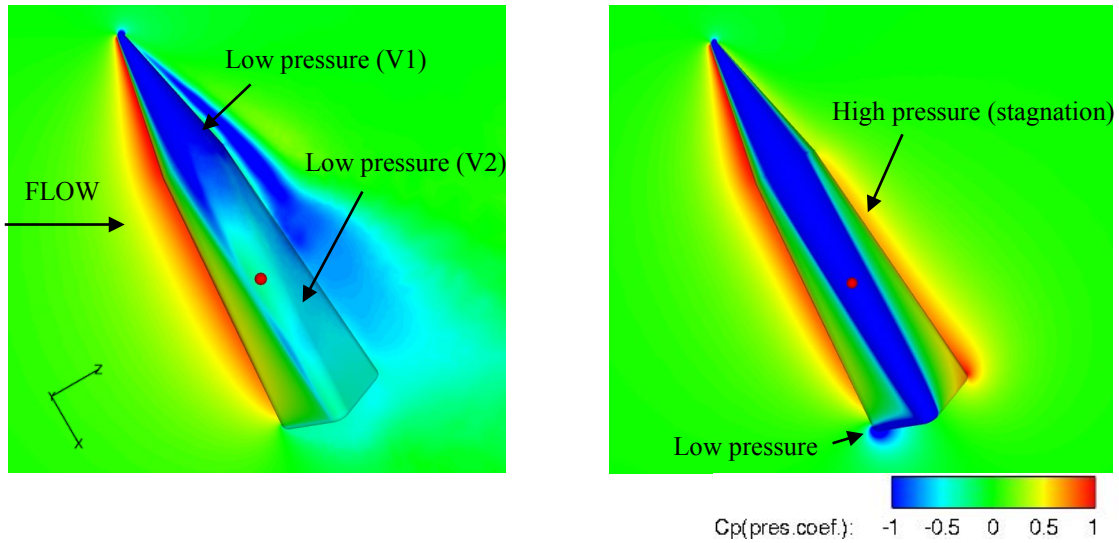


Fig. 21 Pressure distribution (AOA=60 degrees)

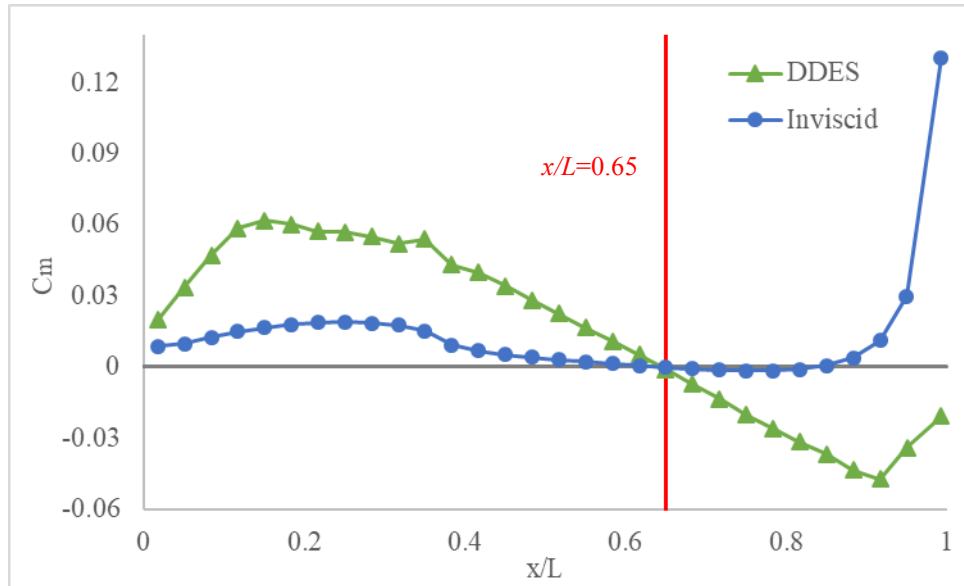


Fig. 22 Local pitching moment distribution (AOA=60 degrees)

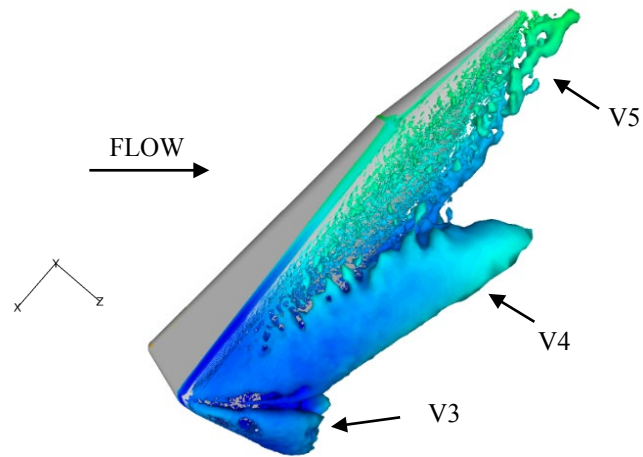


Fig. 23 Q isosurface (AOA=130 degrees)

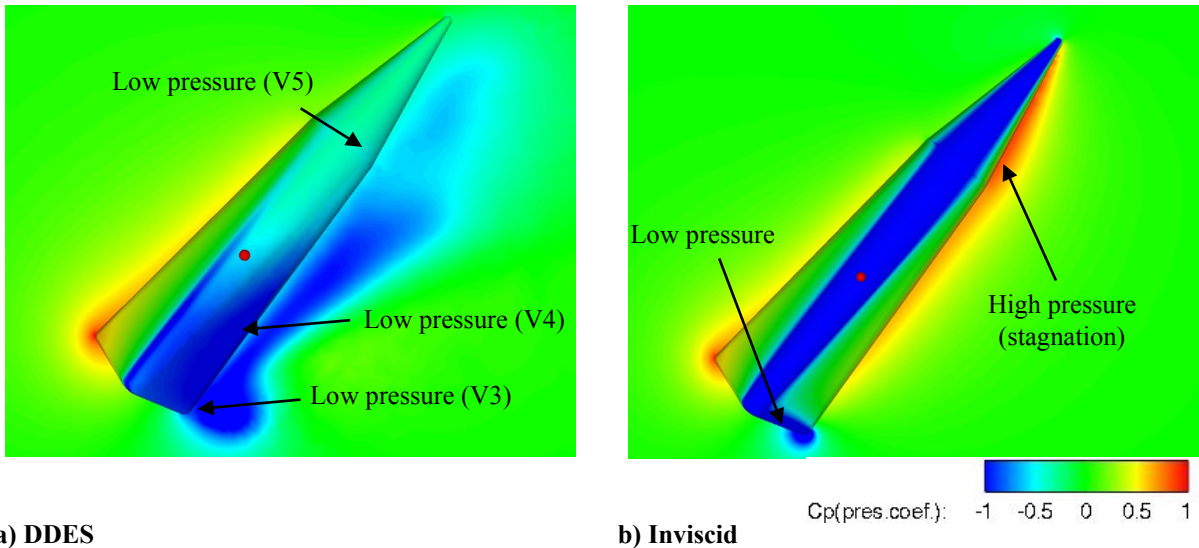


Fig. 24 Pressure distribution (AOA=130 degrees)

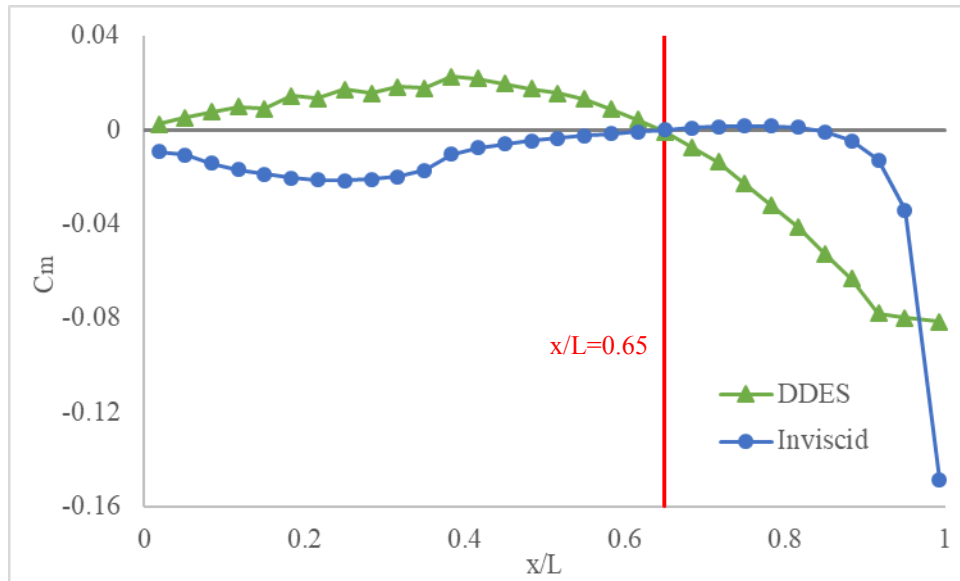


Fig. 25 Local pitching moment distributions (AOA=130 degrees)

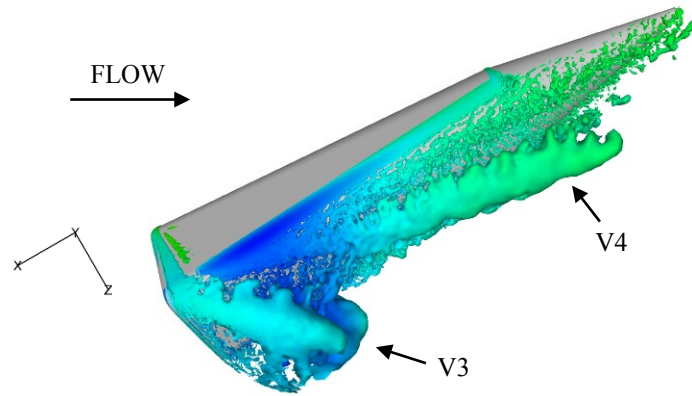
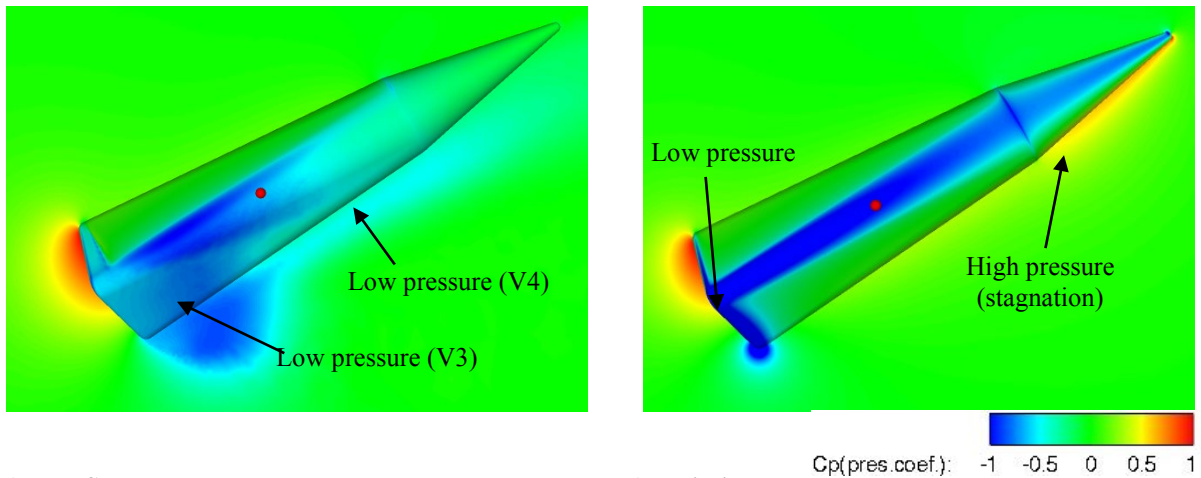


Fig. 26 Q isosurface (AOA=150 degrees)



a) DDES

b) Inviscid

Fig. 27 Pressure distribution (AOA=150 degrees)

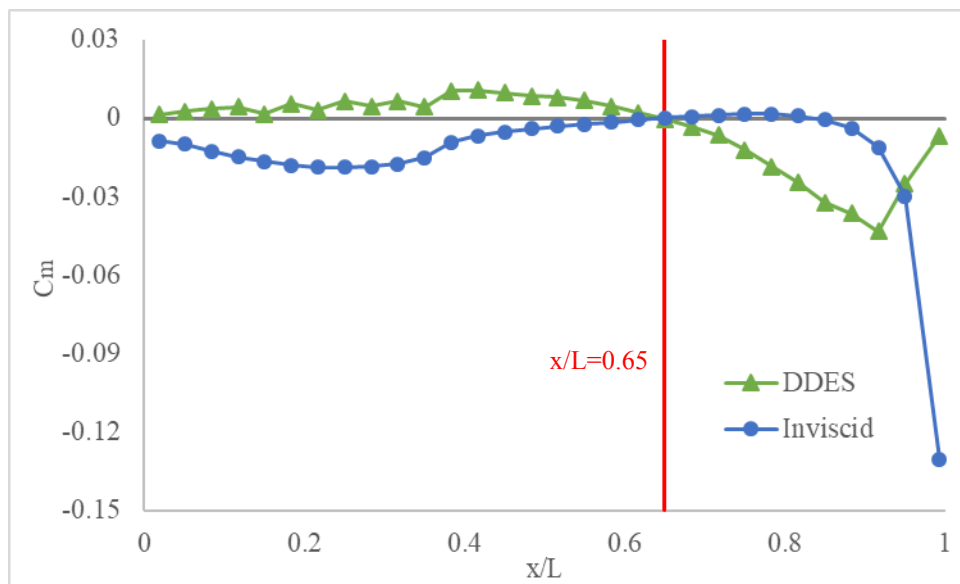


Fig. 28 Local pitching moment distributions (AOA=150 degrees)

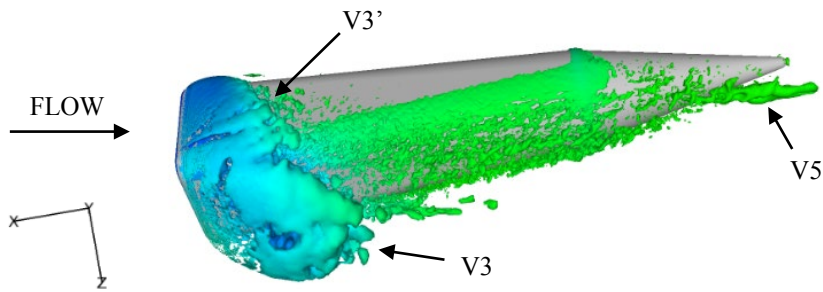
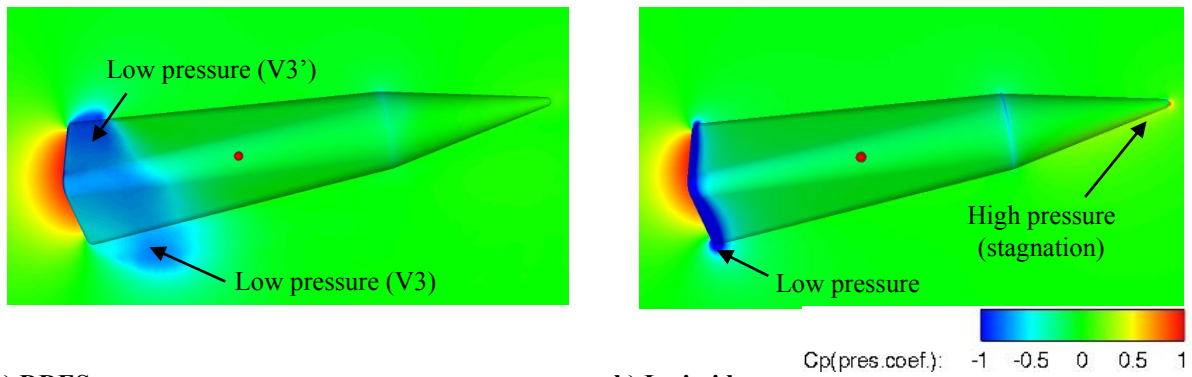


Fig. 29 Q isosurface (AOA=170 degrees)



a) DDES

b) Inviscid

Fig. 30 Pressure distribution (AOA=170 degrees)

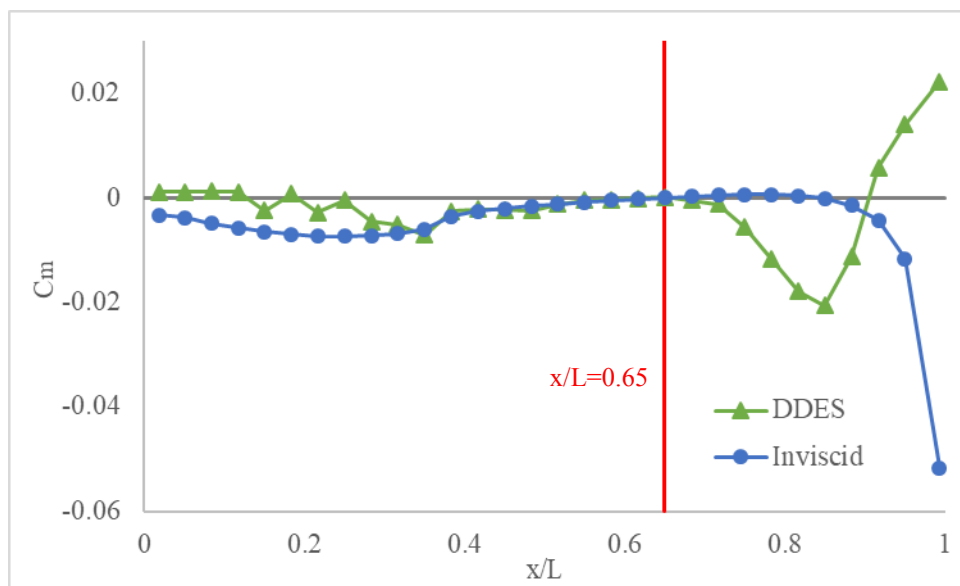
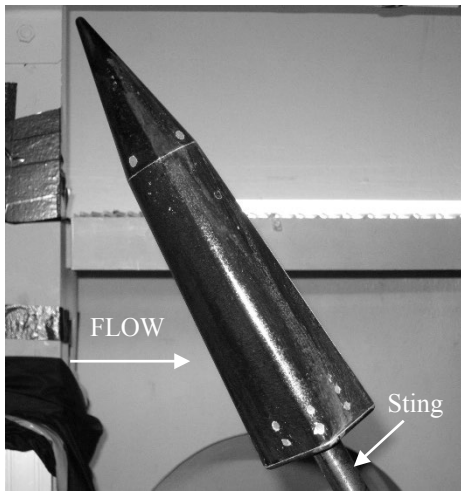
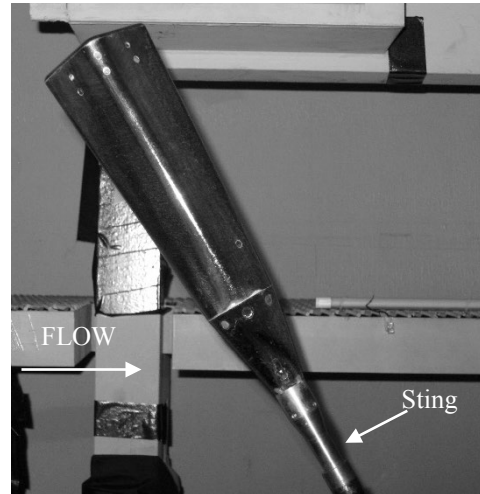


Fig. 31 Local pitching moment distributions (AOA=170 degrees)



a) Forward angles



b) Backward angles

Fig. A1 Model installed in a wind tunnel

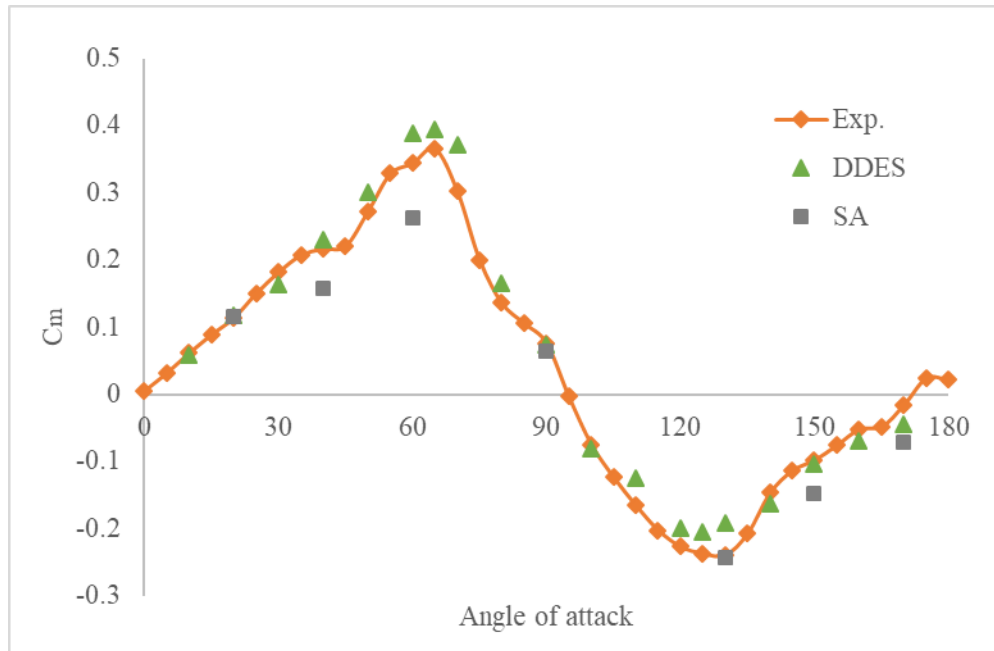


Fig. A2 Pitching moment coefficients (RANS and DDES)

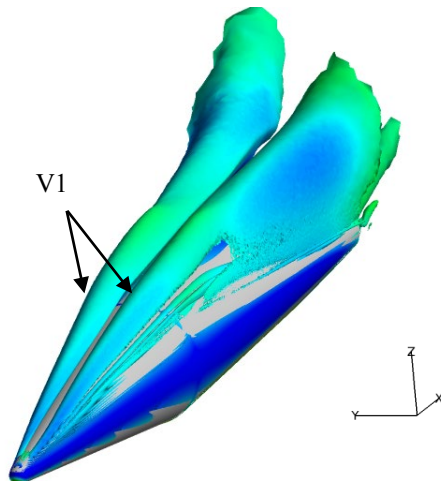


Fig. A3 Q isosurface obtained from RANS (AOA=40 degrees)

Tables

Table 1 Grid dependency study

Grid	Number of nodes	C_m
fine	49.70 million	0.39
medium	31.77 million	0.39
coarse	19.71 million	0.37

Table 2 Computational cases

Case	Angle of attack, degrees
Forward angles	20, 30, 40, 50, 60, 65, 70, 80, 90
Backward angles	100, 110, 120, 125, 130, 140, 150, 160, 170